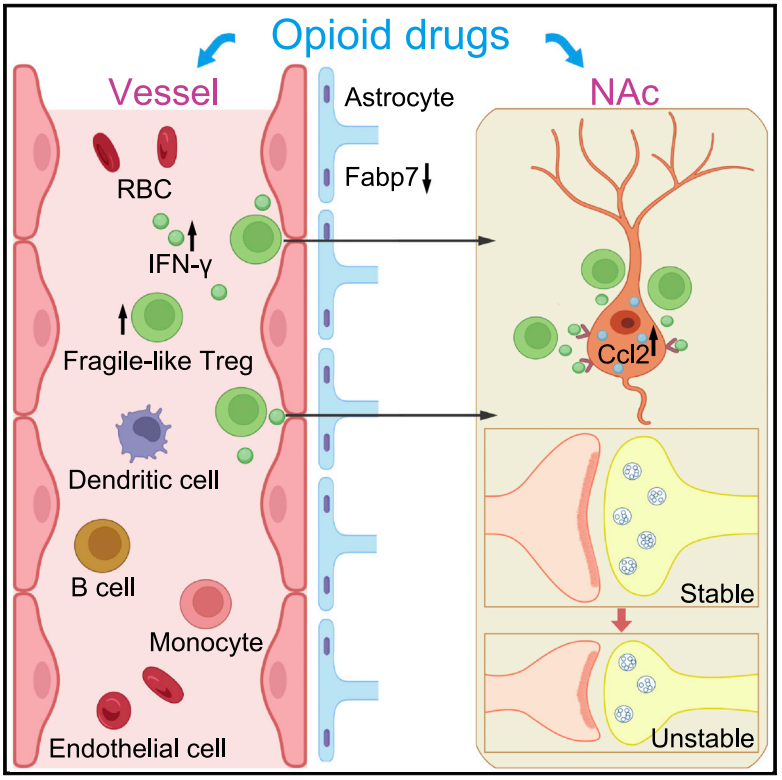
Cell

Opioid-induced fragile-like regulatory T cells contribute to withdrawal

Graphical abstract



Highlights

- An expansion of fragile-like Tregs is identified in heroin-associated blood
- Opioid-induced global hypoxia triggers Treg fragility
- Fabp7 protects BBB integrity from opioid-induced hyperpermeability
- IFN-γ regulates opioid-induced NAc synaptic remodeling and withdrawal signs

Authors

Yongsheng Zhu, Peng Yan, Rui Wang, ..., Xiaoyu Chen, Qing Liang, Kejia Wang

Correspondence

liangqing@xmu.edu.cn (Q.L.), wangkejia@xmu.edu.cn (K.W.)

In brief

Opioids drive the peripheral expansion of fragile-like regulatory T cells that cross the blood-brain barrier and, through IFN-γ, mediate synaptic instability and subsequent withdrawal symptoms.

Zhu et al., 2023, Cell *186*, 591–606
February 2, 2023 © 2022 Elsevier Inc.
https://doi.org/10.1016/j.cell.2022.12.030

CellPress

Cell

CellPress

Article

Opioid-induced fragile-like regulatory T cells contribute to withdrawal

Yongsheng Zhu,[1,11] Peng Yan,[1,11] Rui Wang,[2,3,4] Jianghua Lai,[1] Hua Tang,[5] Xu Xiao,[3,4] Rongshan Yu,[3,4] Xiaorui Bao,[2,3] Feng Zhu,[6] Kena Wang,[1] Ye Lu,[1] Jie Dang,[7] Chao Zhu,[8] Rui Zhang,[9] Wei Dang,[10] Bao Zhang,[1] Quanze Fu,[2,3] Qian Zhang,[2,3] Chongao Kang,[2,3] Yujie Chen,[2,3] Xiaoyu Chen,[2,3] Qing Liang,[2,3,*] and Kejia Wang[2,3,12,*]

[1]National Biosafety Evidence Foundation, Bio-evidence Sciences Academy, Western China Science and Technology Innovation Harbor, Xi'an Jiaotong University, Xi'an, Shaanxi 710115, China

[2]Fujian Provincial Key Laboratory of Organ and Tissue Regeneration, Xiamen Key Laboratory of Regeneration Medicine, Organ Transplantation Institute of Xiamen University, School of Medicine, Xiamen University, Xiamen, Fujian 361102, China

[3]National Institute for Data Science in Health and Medicine, School of Medicine, Xiamen University, Xiamen, Fujian 361102, China

[4]School of Informatics, Xiamen University, Xiamen, Fujian 361005, China

[5]Xi'an International Medical Center Hospital, Xi'an, Shaanxi 710117, China

[6]Center for Translational Medicine, the First Affiliated Hospital of Xi'an Jiaotong University, Xi'an, Shaanxi 710061, China

[7]School of Basic Medicine, Ningxia Medical University, Yinchuan, Ningxia 750004, China

[8]Department of Nephrology, Changhai Hospital, Second Military Medical University, Shanghai 200433, China

[9]Department of Emergency Medicine, Xiang'an Hospital of Xiamen University, School of Medicine, Xiamen University, Xiamen, Fujian 361102, China

[10]The Sixth Ward, Xi'an Mental Health Center, Xi'an, Shannxi 710100, China

[11]These authors contributed equally

[12]Lead contact

*Correspondence: liangqing@xmu.edu.cn (Q.L.), wangkejia@xmu.edu.cn (K.W.)

https://doi.org/10.1016/j.cell.2022.12.030

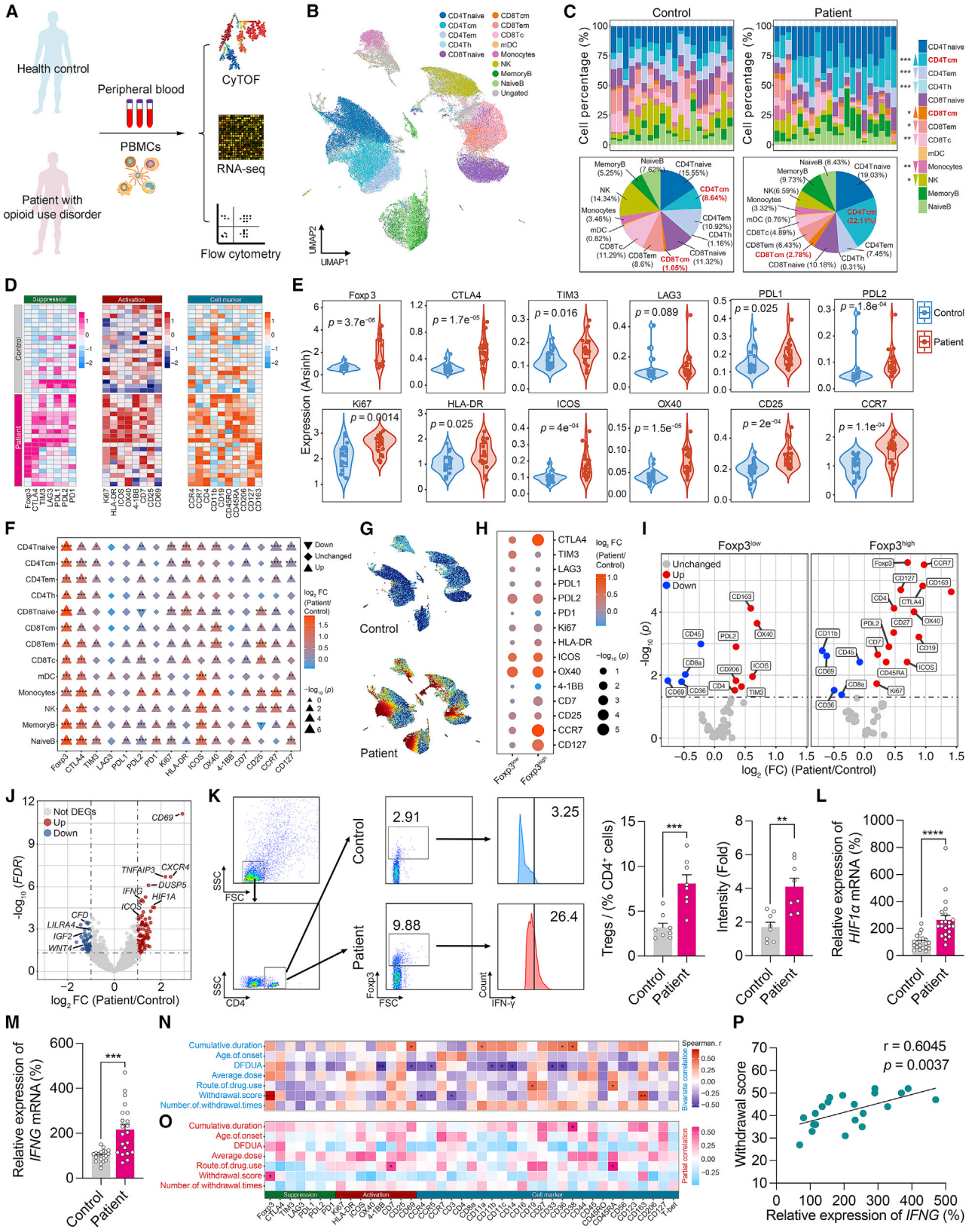
SUMMARY

Dysregulation of the immune system is a cardinal feature of opioid addiction. Here, we characterize the landscape of peripheral immune cells from patients with opioid use disorder and from healthy controls. Opioid-associated blood exhibited an abnormal distribution of immune cells characterized by a significant expansion of fragile-like regulatory T cells (Tregs), which was positively correlated with the withdrawal score. Analogously, opioid-treated mice also showed enhanced Treg-derived interferon-γ (IFN-γ) expression. IFN-γ signaling reshaped synaptic morphology in nucleus accumbens (NAc) neurons, modulating subsequent withdrawal symptoms. We demonstrate that opioids increase the expression of neuron-derived C-C motif chemokine ligand 2 (Ccl2) and disrupted blood-brain barrier (BBB) integrity through the downregulation of astrocyte-derived fatty-acid-binding protein 7 (Fabp7), which both triggered peripheral Treg infiltration into NAc. Our study demonstrates that opioids drive the expansion of fragile-like Tregs and favor peripheral Treg diapedesis across the BBB, which leads to IFN-γ-mediated synaptic instability and subsequent withdrawal symptoms.

INTRODUCTION

Opioid drugs are powerful analgesics, but they are also the most addictive because of their powerful euphoria-inducing effects. The nucleus accumbens (NAc) is a primary site that orchestrates both reward and aversion processes and is thus a promising therapeutic target for treating drug addiction.[1,2] Morphine-induced morphological remodeling in NAc is involved in behavioral sensitization,[3] dependence[4] and withdrawal.[5] However, NAc structural plasticity from damage to recovery, whereby neuronal synapses form new connections to break, remains enigmatic. Morphine-induced increases in leukocyte-endothelial adhesion are accompanied by elevated levels of inflammatory cytokines, which alter blood-brain barrier (BBB) homeostasis and permeability, and exacerbate neuroinflammation.[6] Despite all this knowledge, whether peripheral immune cells and their secreted cytokines interact with the central nervous system (CNS) to modulate synaptic structure or addictive behavior remains largely unknown.

Regulatory T cells (Tregs) are a specialized T cell lineage and have a pivotal function in immunosuppression. Interestingly, a high proportion of so-called fragile Tregs has been found in the tumor microenvironment, which boosts antitumor immunity.[7] Unlike stable Tregs, fragile Tregs are defined as retaining Foxp3 expression but with loss of suppressive function. They can produce interferon-γ (IFN-γ) as a result of elevated HIF1α



(legend on next page)

expression due to hypoxia.[7,8] So far, cells with the fragile Treg phenotype have only been reported in the tumor microenvironment, but whether they occur in other disease states, and what their function is, remain poorly understood.

Here, we report an expanded fragile-like Treg population, characterized by secretion of IFN-γ and sustained HIF1α expression, in patients with opioid use disorder. Subsequently, a similar subset was also found in the blood and NAc of mice after opioid administration. In addition, fragile-like Treg-produced IFN-γ causes synaptic dysfunction and subsequent withdrawal symptoms. We further identified the molecular mechanism by which fragile-like Tregs pass through the BBB.

RESULTS

The presence of fragile-like Tregs subset in patients with opioid use disorder

Cytometry by time of flight (CyTOF) and bulk RNA-seq were performed on peripheral blood mononuclear cells (PBMCs) to investigate immune signatures in 21 patients with opioid use disorder and 20 healthy controls. Flow cytometry was used to verify the results of CyTOF and RNA-seq (Figure 1A). A 41-marker panel was established for immunophenotyping, including markers for immune checkpoints, proliferation, and innate and adaptive immune cells (Table S1). Thirteen cell clusters were exported for dedicated manually gated analyses across all subjects (Figures 1B and S1A). Relative to controls, opioid-associated blood had proportionally increased fractions of $CD4^+$ and $CD8^+$ central memory T cells (Tcm) and decreased $CD4^+$ effector memory T cells (Tem), $CD4^+$ helper T cells (Th), $CD8^+$ Tem, $CD8^+$ cytotoxic T cells (Tc), natural killer (NK) cells, and monocytes (Figures 1C and S1B; Table S1). Unexpectedly, we identified an obvious increase in the expression of a variety of dysfunctional or "exhausted" T cell markers (CTLA4, TIM3, LAG3, PDL1, and PDL2), as well as activation or proliferation markers (HLA-DR, ICOS, CD25, OX40, and Ki67), in opioid-associated blood (Figures 1D and 1E). Furthermore, differences in immune signatures among the different cell subsets were observed between two groups. The analysis of peripheral blood from patients with opioid use disorder revealed that multiple inhibitory markers and activation markers were enhanced in different immune cell subsets (Figure 1F; Table S1). Taken together, these results suggest that opioid exposure may hyperactivate the immune system, leading to dysfunctionality.

As noted, Foxp3, which was broadly co-expressed in various cell subsets, was markedly increased in opioid-associated blood (Figure 1G). Unlike classical $Foxp3^{high}$ cells ($CD4^+$, $CD25^+$, $CTLA4^+$, and $CD127^-$), opioid-associated $Foxp3^{high}$ cells co-expressed CCR7, CD45RA, CD163, CTLA4, CD127, CD4, ICOS, OX40, and Ki67, suggesting a mononuclear, proliferative, and naive phenotype (Figures 1H, 1I, and S1C; Table S1). To further understand gene-expression changes, we performed bulk RNA-seq on PBMCs (Table S2). The expression of a range of cytokine genes (including *IFNG* and *CCL4*) and genes indicating cellular activation (*ICOS*, *CD69*, *MYC*, and *PCNA*) was elevated in PBMCs from patients with opioid use disorder (Figures 1J and S1D). Differentially expressed genes were also enriched in the "T cell receptor (TCR) signaling pathway" and "T cell differentiation" gene sets (Figures S1E and S1F; Table S2). To validate these findings, the phenotype of the $Foxp3^+$ cells was further verified by flow cytometry. Consistent with CyTOF and RNA-seq results, flow cytometry analysis showed that Tregs ($CD4^+$ and $Foxp3^+$) and the IFN-γ they produced were elevated in opioid-associated blood (Figure 1K), while no obvious change of IFN-γ level was observed in other cell subsets (Figure S1G). Moreover, IFN-γ^+ cells were gated to identify that elevated IFN-γ mainly originated from Tregs (Figure S1H). Gating based on the Treg phenotype identified enhanced *HIF1α* and *IFNG*

Figure 1. Identification of peripheral immune milieu in patients with opioid use disorder

(A) Schematic diagram of sample analysis methodology. PBMCs from patients with opioid use disorder and controls were assessed by CyTOF, RNA-seq, and flow cytometry.

(B) Uniform Manifold Approximation and Projection (UMAP) plot of the gated immune cells (4,000 cells per sample; 164,000 cells for all) overlaid with color-coded clusters (n = 41).

(C) Comparison of the percentage of immune cell subsets. Upper panel indicates the percentage in individuals. Lower panel indicates the average of the percentage in groups (n = 20, 21).

(D) Heatmap of immune suppression (left), activation (middle), and cell type (right) markers from all cells (n = 20, 21).

(E) Comparison of the immune suppressive (upper) and activated (lower) markers (n = 20, 21).

(F) Comparison of expression of the indicated markers in different immune cell subsets (n = 20, 21).

(G) The UMAP plot of Foxp3 abundance (n = 20, 21).

(H and I) $Foxp3^{high}$ cells were defined as cells with expression values higher than the mean of total cells, while others are $Foxp3^{low}$ cells. (H) The bubble plot and (I) volcano plot showing the difference between $Foxp3^{high}$ and $Foxp3^{low}$ cells (n = 20, 21).

(J) The volcano plot of PBMCs RNA-seq fold-change values. The red dots represent significantly upregulated DEGs, and the blue dots represent significantly downregulated DEGs (n = 20, 21).

(K) PBMCs samples were verified by flow cytometry. Gating strategy defining Tregs population and Treg-secreted IFN-γ (left). The percentage of Tregs in total $CD4^+$ cells. The fluorescence intensity of Treg-secreted IFN-γ (right) (n = 8).

(L and M) Tregs populations were sorted by fluorescence-activated cell sorting. Comparison of the relative expression of (L) *HIF1α* and (M) *IFNG* mRNA in Tregs (n = 20, 21).

(N and O) Correlation between CyTOF markers expression and addiction-related traits in patients with opioid use disorder by (N) bivariate correlation and (O) partial correlation analysis (n = 21). DFDUA, duration from first drug use to addiction.

(P) Correlation analysis between the withdrawal score and the relative expression of Treg-derived *IFNG* (n = 21).

In (E) violin plots showing the distribution of arcsinh-transformed marker expression values, boxplots inside violin plots are shown as the median ± 25%–75% quantiles, and whiskers denote 1.5× interquartile range (IQR); (K, L, and M) Data are shown as mean ± SEM. Data represent four to five independent experiments. $^{**}p < 0.01$, $^{***}p < 0.001$, $^{****}p < 0.0001$.

See also Figure S1 and Tables S1 and S2.

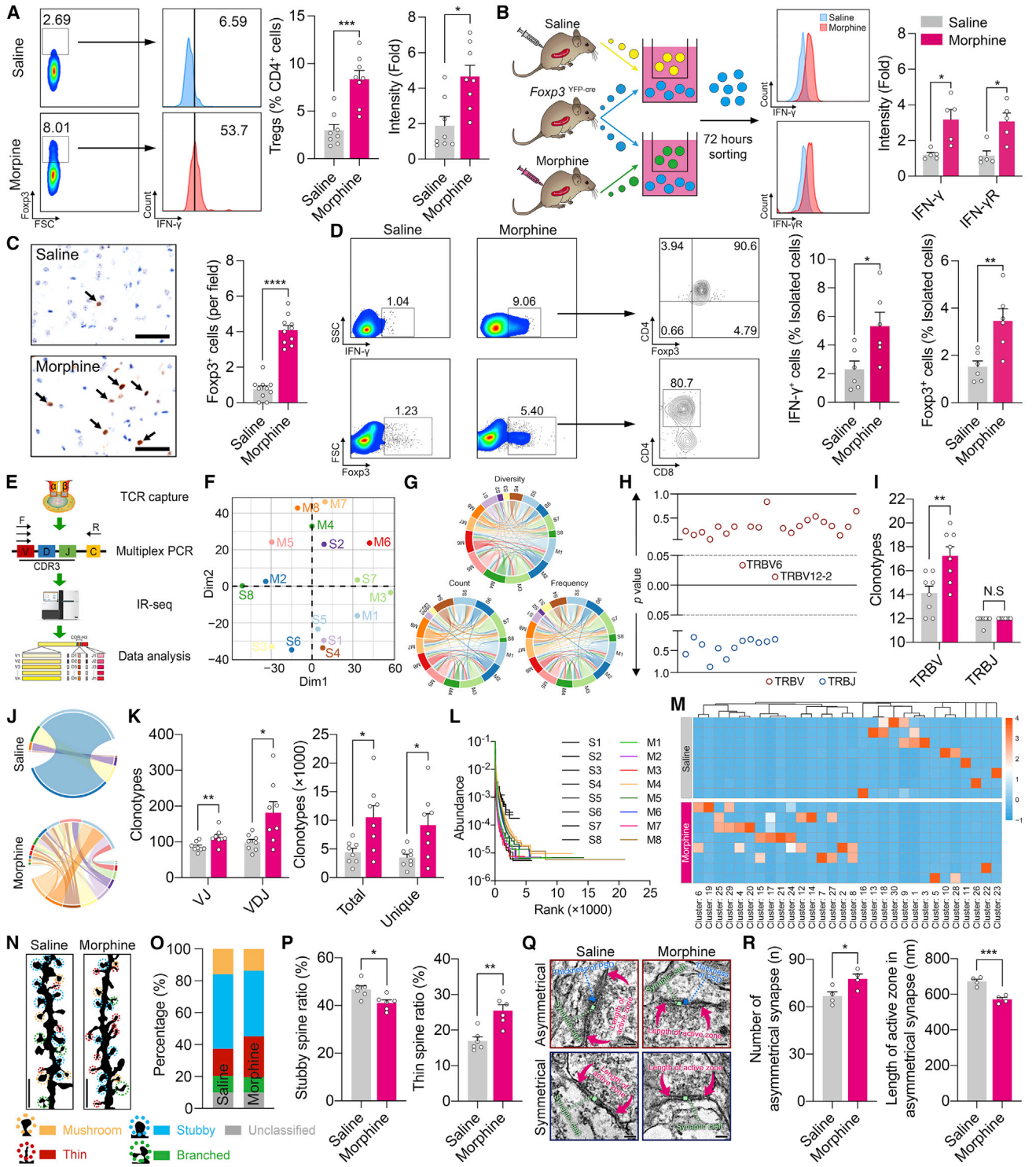


Figure 2. Opioids administration causes fragile-like Treg infiltration and synaptic plasticity in NAc

(A) The mice were treated with morphine as described in Figure S2A. Representative plots of Tregs and IFN-γ in PBMCs by flow cytometry (left). The percentage of Tregs. The fluorescence intensity of Treg-gated IFN-γ (right) (n = 8).

(B) Tregs were isolated from spleens of mice noted, stimulated with PMA, ionomycin, and IL-2, and co-cultured for 72 h. Representative histogram plots (left) and quantification (right) of the intensity of IFN-γ and IFN-γR (n = 5).

(C) Representative images (left) and quantification (right) of Foxp3 immunoreactivity in NAc (n = 10); scale bars, 50 μm.

(legend continued on next page)

expression by these cells in opioid-associated blood (Figures 1L and 1M), indicating the appearance of a fragile-like Treg subset.

To explore the potential biological role of opioid-associated fragile-like Tregs, we performed correlation analyses of the above results and addiction-related traits in patients with opioid use disorder. The correlations of cell-marker expression were first investigated, and we identified a significant positive correlation between Foxp3 and CD163 (Figure S1I). Subsequently, we systematically elucidated the relationship between immune status and opioid addiction phenotypes. Strikingly, there was a positive correlation between Foxp3 expression and withdrawal score (Figures 1N, 1O, and S1J). Moreover, the relative level of expression of Treg-derived *IFNG* positively correlated with withdrawal scores (Figure 1P), indicating that fragile-like Tregs may be involved in opioid-induced withdrawal symptoms.

Opioid-induced hypoxia triggers fragile-like Treg phenotype

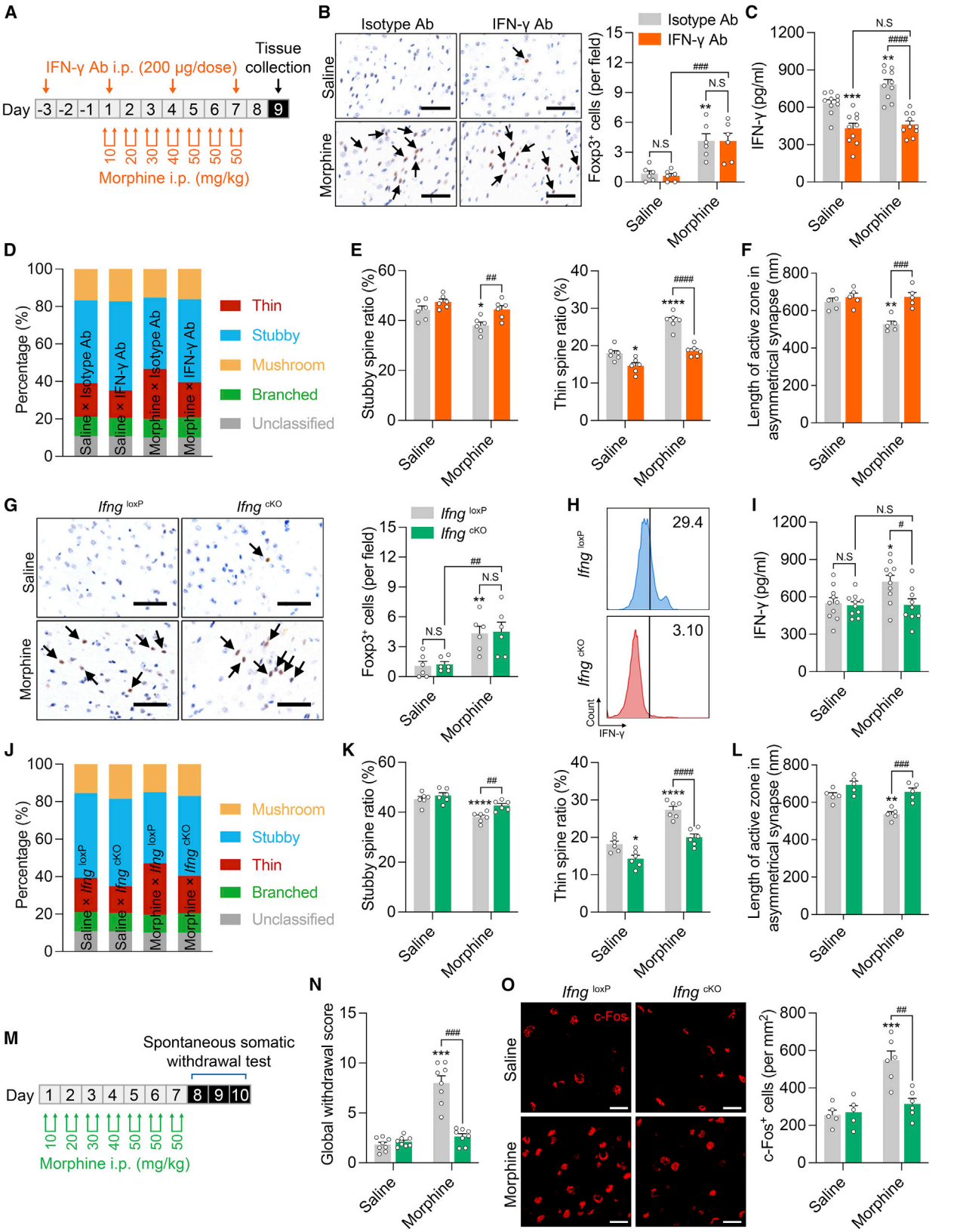
To investigate the effect of opioids in mice, wild-type (WT) mice were given increasing doses of morphine or heroin (Figure S2A). Flow cytometry confirmed that there was an increased percentage of Tregs as well as the level of Treg-derived IFN-γ and T-box transcription factor 21 (T-bet) in various organs (blood, thymus, spleen, abdominal lymph nodes, and liver) after morphine treatment (Figures 2A and S2B). However, morphine treatment had no effect on the expression of IFN-γ in $CD8^+$ T cells and $Foxp3^-$ $CD4^+$ T cells (Figure S2C). Treg fragility is defined by a dominant effect of fragile Tregs on WT Tregs. Moreover, IFN-γ is required and sufficient to drive Treg fragility.[7] To test if opioid-mediated fragile-like Tregs could directly impact the function of WT Tregs, we co-cultured splenic Tregs from $Foxp3^{YFP\text{-}cre}$ mice (with or without opioid-drug treatment) (Figure S2D). Indeed, WT Tregs that were co-cultured with opioid-mediated fragile-like Tregs enhanced the expression levels of IFN-γ and IFN-γ receptor (IFN-γR) and drove Treg fragility (Figures 2B and S2E). $Foxp3^+$ cell-specific IFN-γ knockout ($Ifng^{cKO}$) mice were also used to verify Treg fragility (Figure S2F). Elimination of IFN-γ reduced morphine-induced expression of T-bet and IFN-γR *in vivo* (Figure S2G–S2I). These data indicate a critical role of IFN-γ produced by fragile-like Treg in mediating Treg transformation.

As mentioned above, opioid-mediated Treg fragility is a global effect. In order to identify which factor triggers Treg transformation, the WT Tregs were treated with different concentrations of morphine or heroin for 72 h *ex vivo*. We found that opioid treatment had no effect on the expression levels of Treg-derived IFN-γ and T-bet, indicating that opioids could not directly drive Treg fragility (Figures S2J and S2K). A study has supported the notion that intratumorally mediated hypoxia facilitates Treg fragility.[7] The monitoring of arterial oxygen saturation (SaO_2) was conducted in mice after opioid treatment. Indeed, opioids caused a reduction in SaO_2 (Figure S2L); this may have an exert effect on opioid-associated respiratory depression and hypoxia.[9–11] Western blotting also revealed upregulation of Hif1α and p-Akt (S473) and downregulation of Foxo3a and Foxo1 in Tregs from opioid-treated mice, suggesting that Akt/Hif1α axis could prime Tregs to become fragile-like in hypoxic conditions (Figures S2M and S2N). Taken together, these results demonstrate that Treg fragility transformation is primarily due to opioid-induced global hypoxia rather than its direct pharmacological effect.

Opioids lead to fragile-like Treg infiltration and synaptic plasticity in NAc

Enzyme-linked immunosorbent assay (ELISA) documented elevated IFN-γ expression both in blood and in NAc after morphine or heroin treatment (Figure S3A). Of note, we detected a sizeable population of $Foxp3^+$ cells in NAc from opioid-treated mice (Figures 2C, 2D, and S3B–S3E), and the expanded IFN-γ^+ cells displayed a signature of $CD4^+$ $Foxp3^+$ Tregs (Figure 2D). Obviously, morphine-induced IFN-γ augments mainly originated from $CD4^+$ $Foxp3^+$ Tregs rather than from $Foxp3^+$ $CD4^-$ cells and $Foxp3^-$ cells in NAc (Figure S3F). Moreover, very little positive staining of B cell marker (CD19), NK cell marker (NK1.1), and monocyte cell marker (Ly6c) was detected after morphine treatment (Figure S3G). The levels of other inflammatory factors (IL-6,

(D) NAc-derived cell suspensions were prepared. The samples were analyzed for the expression of IFN-γ, Foxp3, CD4, and CD8 markers. Contour plots showing the cell populations from the indicated gates (left). The percentage of IFN-γ^+ cells and $Foxp3^+$ cells (right) (n = 6).
(E) Capturing the TCR in NAc. Flow chart of the TCR IR-seq design and analysis.
(F–M) Analysis of TCR β chain frequency and diversity in NAc.
(F) Principal component analysis (PCA) showing the closeness of CDR3 aa usage.
(G) Circle diagrams representing the overlap of the CDR3 aa count, frequency, and diversity.
(H) Comparison of the frequency of V and J segments.
(I) The compositions of the V and J segments.
(J) Representative circle diagrams of the VJ pair segments.
(K) The clonotypes of VJ, VDJ (left), and total and unique CDR3 aa (right).
(L) The rank abundance showing the diversity of CDR3 aa clonotypes.
(M) Heatmap of the hierarchical clustering of CDR3 aa clusters (n = 8).
(N–P) The dendritic spines morphological changes of MSNs in NAc by Golgi-Cox staining.
(N) Representative images of dendritic spines on secondary dendrites of MSNs in NAc. The dendritic spines were categorized into mushroom-, stubby-, thin-, and branched-like spines; scale bars, 5 μm.
(O) Histograms showing the distribution of different spine types.
(P) The proportions of stubby-like (left) and thin-like (right) spines (n = 6).
(Q and R) The synaptic morphological changes of NAc by TEM.
(Q) Representative images of asymmetric and symmetric synapses in Nac; scale bars, 100 nm.
(R) The number of asymmetrical synapses (left) and the lengths of active zones of asymmetrical synapses (right) (n = 4).
Data are shown as the mean ± SEM. Data represent three to five independent experiments. *p < 0.05, **p < 0.01, ***p < 0.001, ****p < 0.0001.
See also Figures S2–S4 and Table S3.



(legend on next page)

TNF-α, and IL-17) and Treg-associated cytokines (TGF-β and IL-10) were reduced or remained unchanged in the blood and NAc of opioid-treated mice (Figures S3H and S3I). These results indicate that IFN-γ upregulation is specific to $CD4^+$ $Foxp3^+$ Treg infiltration into NAc.

TCR repertoire and signal play an important role in regulating Treg differentiation, homeostasis, and function. The amino-acid (aa) clonotype of the complementarity-determining region 3 (CDR3) region of the TCR β chain determines the origin and diversity of T cell clones.[12] To investigate whether the infiltrating T cells originate from peripheral blood or from the proliferation of resident T cells in NAc, the TCR β chain clonotypes were tracked by IR-seq (Figure 2E). A total of 23 V segments, 12 J segments, 200 VJ segments, 306 VDJ segments, and 82,075 distinct CDR3 aa clonotypes was identified from all NAc samples (Table S3). Morphine exposure resulted in a significantly different CDR3 aa profile (Figure 2F) due to decreased counts, frequencies, and diversity of overlapping CDR3 aa clonotypes between the two groups (Figures 2G and S4A). Although the frequency patterns of most V, J, VJ, VDJ, and CDR3 aa in the two groups were similar (Figures 2H and S4B–S4D), expanded V, VJ, VDJ, and CDR3 aa clonotypes were detected after morphine treatment (Figures 2I–2K). There was a significantly higher diversity of CDR3 aa clonotypes in NAc after morphine treatment (Figures 2L, 2M, and S4E). These data reveal that opioids induce peripheral T cell infiltration rather than the proliferation of resident T cells in NAc.

To investigate the effect of opioids on NAc synaptic plasticity, we first quantified neurons in NAc. Morphine treatment did not affect the number of neurons (Figure S4F). Consistent with these results, both cell apoptosis and necroptosis remained unchanged after morphine exposure (Figures S4G and S4H). A study has showed that thin-like spines are increased in medium spiny neurons (MSNs) in NAc 1 day after morphine withdrawal.[13] In our study, dendritic spines were categorized as mushroom-, stubby-, thin-, or branched-like spines[14] (Figure S4I). The total spine density of MSNs in NAc was not altered after 7 days of morphine administration (Figure S4J). The proportions of stubby-like spines and thin-like spines were decreased and increased, respectively, in the morphine-treated group (Figures 2N–2P), which indicated that immature/unstable synaptic structures of MSNs were increased after morphine exposure. The numbers of synapses and symmetrical synapses were also found not to be affected after 7 days of morphine administration (Figure S4K). The numbers of asymmetrical synapses and the lengths of active zones of these synapses, however, were increased and decreased, respectively, in morphine-treated mice (Figures 2Q and 2R), which indicated excitatory synaptic function was weakened. Subsequently, the long-term morphine treatment regimen also revealed analogous changes in NAc (Figures S4L–S4S). These results on morphological changes show that synapses are weakened in NAc after morphine exposure.

Elimination of IFN-γ prevents NAc synaptic weakening

To determine whether IFN-γ influences synaptic plasticity in NAc, mice were administered an IFN-γ neutralizing antibody (anti-IFN-γ) before morphine treatment (Figure 3A). Blocking IFN-γ did not prevent Treg infiltration (Figure 3B) but decreased IFN-γ levels in NAc (Figure 3C). At the same time, the proportion of stubby-like spines was increased and the proportion of thin-like spines was decreased (Figures 3D, 3E, S5A, and S5B). Moreover, the lengths of active zones of these synapses were increased, suggesting that synapse function was strengthened (Figures 3F, S5C, and S5D). The morphological results suggested that potential synapse-weakening effects were prevented. We further used genetic ablation to investigate whether IFN-γ from $Foxp3^+$ cells alters structural plasticity by examining spine morphology in NAc. As in morphine-treated mice, $Ifng^{cKO}$ mice also showed Treg infiltration into NAc (Figure 3G).

Figure 3. Elimination of IFN-γ prevents morphine-induced NAc synaptic weakening

(A) Flow chart of morphine and anti-IFN-γ antibody administration *in vivo*.

(B and C) The effects of anti-IFN-γ on morphine-mediated Treg infiltration and IFN-γ level in NAc by immunohistochemistry and ELISA.

(B) Representative $Foxp3^+$ cells of immunohistochemistry images; scale bars, 50 μm (left). Quantification of $Foxp3^+$ cells per high-power field (right) (n = 6).

(C) The level of IFN-γ in NAc detected by ELISA (n = 10).

(D–F) The effects of anti-IFN-γ on morphine-mediated synaptic morphology by Golgi-Cox staining and TEM.

(D) Histograms showing the distribution of different spine types.

(E) The proportions of stubby-like (left) and thin-like (right) spines (n = 6).

(F) The lengths of active zones in asymmetrical synapses (n = 5).

(G–I) The $Ifng^{loxP}$ and $Ifng^{cKO}$ mice were treated with morphine as described in Figure S2A. The effects of $Ifng^{cKO}$ on morphine-mediated Treg infiltration and IFN-γ level in NAc by immunohistochemistry, flow cytometry, and ELISA.

(G) Representative $Foxp3^+$ cells of immunohistochemistry images; scale bars, 50 μm (left). Quantification of $Foxp3^+$ cells per high-power field (right) (n = 6).

(H) The fluorescence intensity of Treg-gated IFN-γ by flow cytometry.

(I) The level of IFN-γ detected by ELISA (n = 9, 10).

(J–L) The effects of $Ifng^{cKO}$ on morphine-mediated synaptic morphology in NAc by Golgi-Cox staining and TEM.

(J) Histograms showing the distribution of different spine types.

(K) The proportions of stubby-like (left) and thin-like (right) spines (n = 6).

(L) The lengths of active zones in asymmetrical synapses (n = 5).

(M) Flow chart of morphine-induced spontaneous somatic withdrawal test.

(N) The effects of $Ifng^{cKO}$ on the global withdrawal score 48 h after the last morphine treatment (n = 8).

(O) The immunostaining of c-Fos in NAc; scale bar, 25 μm (left). Quantification of c-Fos^+ cells per mm^2 (right) (n = 5, 6).

Data are shown as the mean ± SEM. Data represent three to five independent experiments. $^*p < 0.05$, $^{**}p < 0.01$, $^{***}p < 0.001$, $^{****}p < 0.0001$ compared with saline × isotype Ab group (B, C, E, and F) or saline × $Ifng^{loxP}$ group (G, I, K, L, N, and O); $^{\#}p < 0.05$, $^{\#\#}p < 0.01$, $^{\#\#\#}p < 0.001$, $^{\#\#\#\#}p < 0.0001$.

See also Figures S5 and S6.

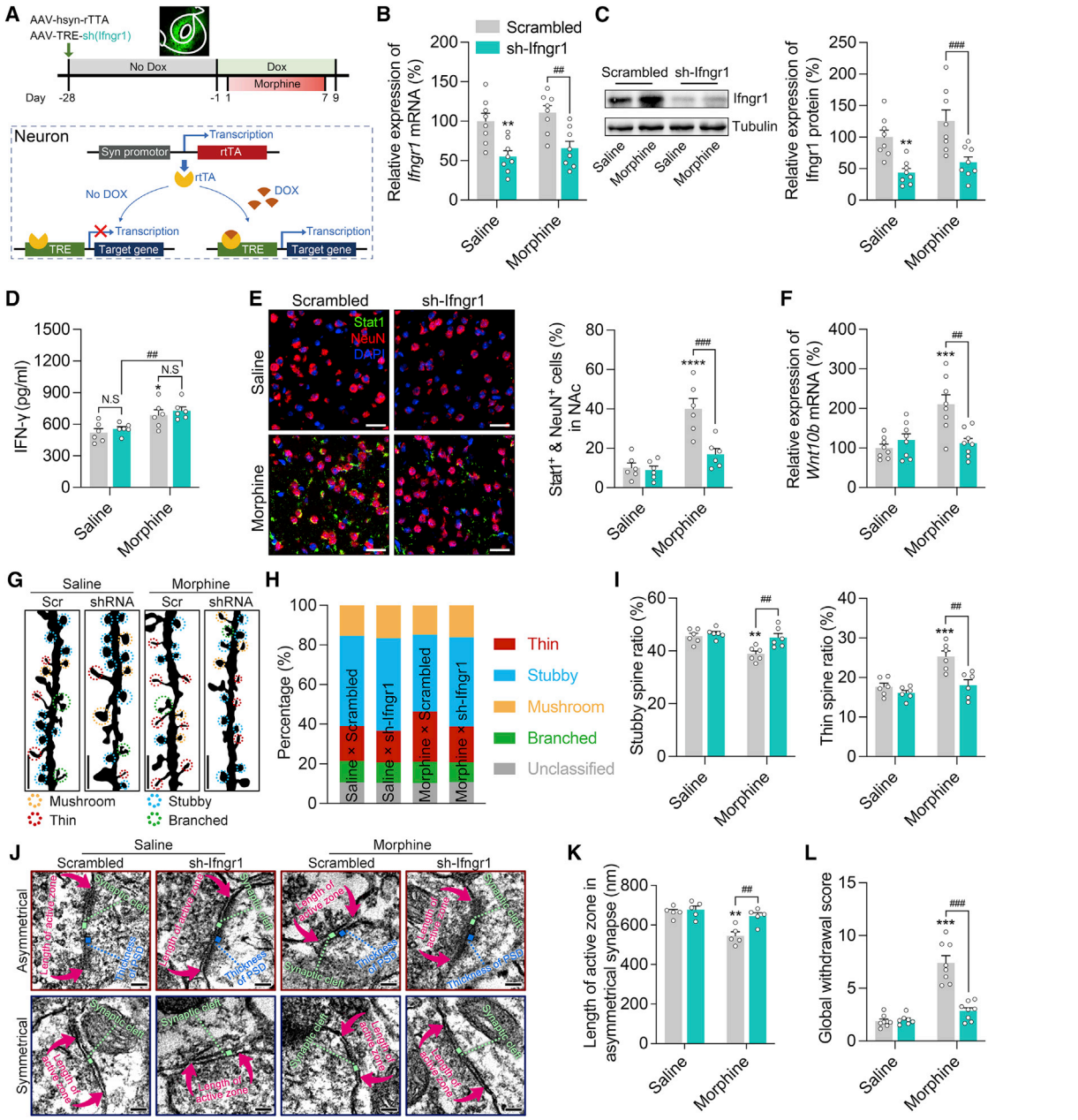


Figure 4. NAc neuronal IFN-γ signaling modulates synaptic plasticity

(A) Flow chart (upper) and schematic (lower) of the specific knockdown of Ifngr1 in NAc neurons using hsyn-driven tet-on system.

(B–D) The qPCR, western blotting, and ELISA showing the efficiency of Ifngr1 knockdown in NAc.

(B) The relative expression level of *Ifngr1* mRNA (n = 8).

(C) Representative images of immunoblots (left). The relative expression level of Ifngr1 protein (right) (n = 8).

(D) The level of IFN-γ by ELISA (n = 6).

(E) Representative co-immunostaining images for Stat1, NeuN, and DAPI in NAc; scale bar, 25 μm (left). The percentage of Stat1 + NeuN double-labeled cells (right) (n = 6).

(F) The relative expression level of *Wnt10b* mRNA (n = 8).

(G–K) The effects of Ifngr1 knockdown on the synaptic structure in NAc by Golgi-Cox staining and TEM.

(G) Representative Golgi-Cox staining images; scale bars, 5 μm.

(H) The distribution of different spine types.

(I) The proportions of stubby-like (left) and thin-like (right) spines (n = 6).

(J) Representative TEM images; scale bars, 100 nm.

(K) The lengths of active zones in asymmetrical synapses (n = 5).

(legend continued on next page)

Nevertheless, the amount of IFN-γ produced by Tregs in NAc was significantly reduced after morphine treatment (Figures 3H and 3I). We observed morphological changes of spines and synapses and detected similar effects with anti-IFN-γ administration. The results showed that morphine-induced synaptic weakening was also prevented in morphine-treated *Ifng*^{cKO} mice (Figures 3J–3L and S5E–S5H). We then tested the effects of IFN-γ at different stages of morphine-conditioned place preference (CPP) (Figure S5I). Interestingly, acquisition and morphine-challenged reinstatement were not prevented in morphine-treated *Ifng*^{cKO} mice (Figure S5J), but the withdrawal symptoms were alleviated from 12 to 60 h in these mice (Figures 3M, 3N, and S5K).

To determine which afferents to NAc were activated in morphine-treated mice, we injected the retrograde tracer fluorogold (FG) into NAc and performed double labeling of c-Fos and FG in the basolateral amygdala (BLA), ventral hippocampus (vHIP), medial prefrontal cortex (mPFC), and paraventricular nucleus of the thalamus (PVT) (Figure S6A). We observed an increase in active c-Fos cells (the ratio of c-Fos+FG to total FG-positive cells) only in PVT in morphine-treated mice (Figures S6B and S6C). We selectively inhibited NAc and PVT→NAc projection in morphine-treated mice via a chemogenetic approach. We found that the inhibition of NAc or PVT→NAc projection significantly ameliorated withdrawal symptoms (Figures S6D–S6G). These data reveal that NAc and its afferent PVT are necessary for morphine-induced withdrawal symptoms.[15] By immunostaining, we also found that c-Fos-positive cells were significantly increased within NAc of morphine-treated *Ifng*^{loxP} mice but not morphine-treated *Ifng*^{cKO} mice (Figure 3O). Altogether, these results show that Treg-mediated IFN-γ is essential for morphine-treatment-induced synaptic weakening and subsequent withdrawal symptoms.

NAc neuronal IFN-γ signaling modulates synaptic plasticity

To assess the role of IFN-γ in neuronal signaling, we decreased the level of IFN-γ receptor R1 (Ifngr1) expression in NAc using an hsyn-driven tet-on system. The AAV-TRE-shRNA (Ifngr1) (downregulation) with AAV-hsyn-rTTA were injected into NAc (Figure 4A). The Ifngr1 shRNA efficiently reduced Ifngr1 expression but not IFN-γ levels (Figures 4B–4D). Immunofluorescence staining revealed an increased expression of Stat1 (the gene responding in the IFN-γ signaling pathway) in NAc after morphine treatment. Enhanced Stat1 was inhibited by the tet-on system when Ifngr1 was downregulated (Figures 4E and S6H). The Wnt family and Bst2, identified as targets of IFN-γ signaling, play key roles in synapse formation and damage.[16,17] To investigate potential molecular mechanisms of the observed effects, we further examined *Wnt10b* and *Bst2* expression in NAc. Indeed, blocking IFN-γ signaling suppressed morphine-induced *Wnt10b* expression (Figure 4F), whereas no significant change of *Bst2* expression was found (Figure S6I). Furthermore, morphine-induced synaptic weakening was prevented when the Ifngr1 was knocked down (Figures 4G–4K, S6J, and S6K). Amelioration of withdrawal symptoms was also observed after blocking IFN-γ signaling (Figures 4L and S6L). Together, these data indicate a necessity for the activation of IFN-γ signaling to induce high synaptic plasticity in NAc after morphine treatment.

Opioids facilitate Ccl2-mediated Treg recruitment

A key question is why Tregs infiltrate into NAc. It may be that NAc chemokine recruitment is a necessary factor. We therefore analyzed the expression of C-C motif chemokine ligand 2 (Ccl2), Ccl19, and Ccl21, which are potential candidate chemokines involved in Treg trafficking.[18,19] We found an increase of Ccl2 expression in NAc after morphine treatment, while there was no significant difference of Ccl2 expression in blood, suggesting that the Ccl2 augmentation was attributable to NAc (Figure 5A). In contrast, morphine treatment did not enhance the expression of Ccl19 and Ccl21 in NAc (Figure S7A). Furthermore, immunofluorescence analysis indicated that the elevated Ccl2 originated from neurons rather than astrocytes (Figures 5B and S7B). To verify whether neuron-derived Ccl2 mediates Treg recruitment, we created Foxp3^{+} cell-specific Ccr2 knockout (*Ccr2*^{cKO}) mice (Figure S7C). Although deletion of Ccr2 in Treg did not alter Ccl2 expression in neurons (Figure 5C), morphine-treated *Ccr2*^{cKO} mice showed less Treg infiltration and lower IFN-γ production and Stat1 expression (Figures 5D–5F). Moreover, morphine-induced synaptic weakening (Figures 5G–5I and S7D–S7G) and withdrawal symptoms (Figures 5J and S7H) were also prevented in *Ccr2*^{cKO} mice.

Interestingly, a study has demonstrated that Stat1 signaling can drive neuronal Ccl2 expression.[20] Thus, Ccl2 and Foxp3 staining was performed to identify the correlation between Stat1 signaling and Ccl2-mediated Treg recruitment. Downregulation of Ifngr1 did not alter morphine-induced Ccl2 and Foxp3 staining, indicating that morphine facilitates neuronal Ccl2 expression and Treg recruitment independent of Stat1 signaling (Figures S7I and S7J), and that this process is associated with opioid-induced Ccl2 production by neurons via μ-opioid receptors.[21]

Fabp7 is essential for opioid-associated BBB hyperpermeability

Morphine treatment significantly altered 248 transcripts in NAc, with a total of 111 upregulated and 137 downregulated (Figure 6A; Table S4). In addition, gene-set-enrichment analysis (GSEA) revealed that morphine mainly affected synaptic transmission-, immune response-, and addiction-related pathways (Table S4). Five differentially expressed genes (DEGs) of interest that were found to be involved in synaptic plasticity or immunologic injury (*Fabp7*, *S100a9*, *Fmo2*, *Hif3a*, and *Wnt10b*) were selected.[22–25] The assessment of the mRNA expression of these genes was in close agreement with that found by RNA-seq analysis, with the exception of *S100a9* (Figures S7K and S7L).

(L) The effects of Ifngr1 knockdown on the global withdrawal score 48 h after the last morphine treatment (n = 7, 8).

Data are shown as the mean ± SEM. Data represent three to five independent experiments. *p < 0.05, **p < 0.01, ***p < 0.001, ****p < 0.0001 compared with saline × scrambled group; $^{\#\#}$p < 0.01, $^{\#\#\#}$p < 0.001.

See also Figure S6.

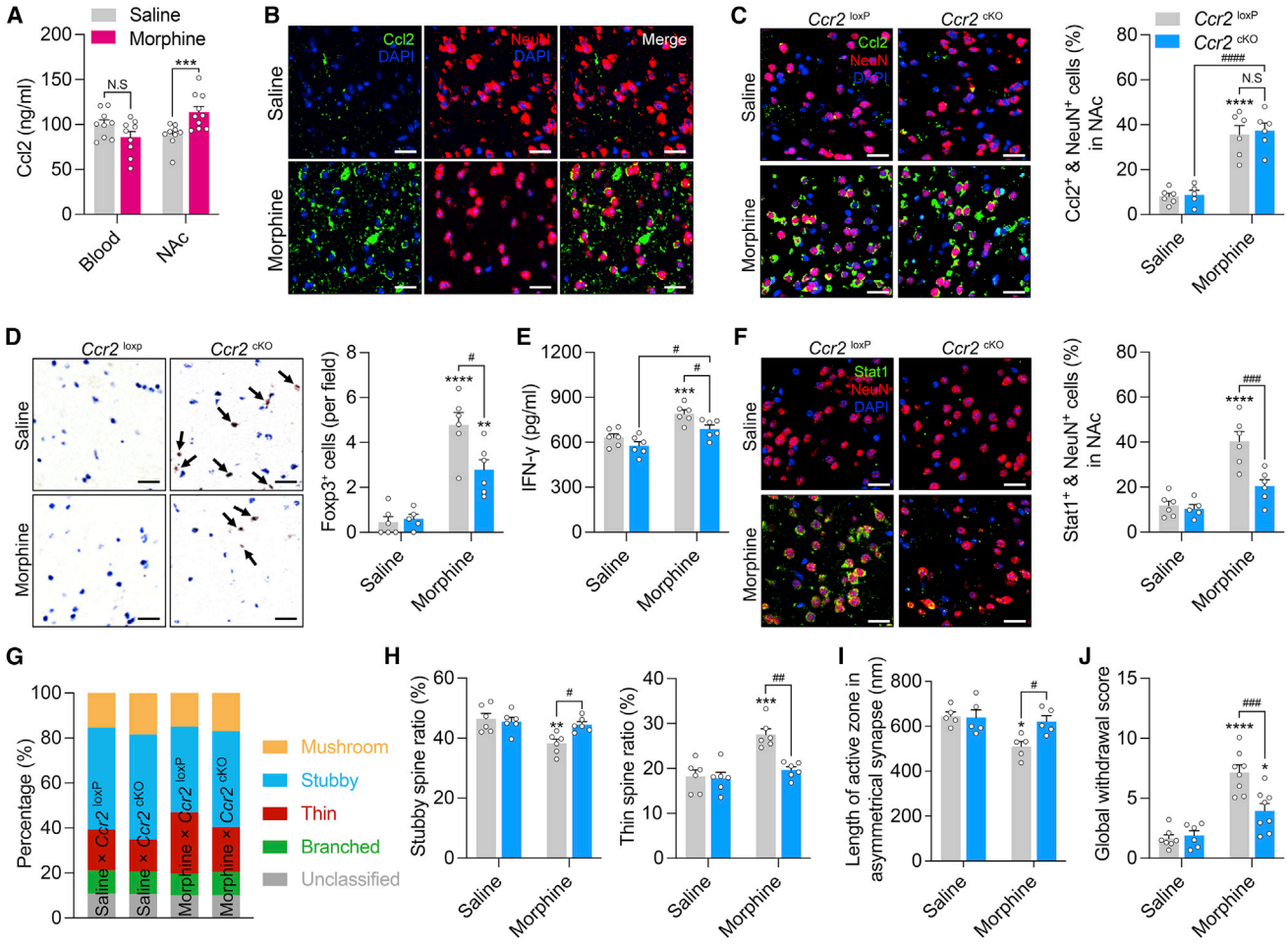


Figure 5. Foxp3^{+}-specific deletion of Ccr2 improves morphine-induced effect in NAc

(A) The levels of Ccl2 in peripheral blood and NAc determined by ELISA (n = 9, 10).

(B) Representative co-immunostaining images for Ccl2, NeuN, and DAPI in Nac; scale bars, 25 μm.

(C–F) The *Ccr2*^{loxP} and *Ccr2*^{cKO} mice were treated with morphine as described in Figure S2A.

(C) Representative co-immunostaining images for Ccl2, NeuN, and DAPI in NAc; scale bars, 25 μm (left). The percentage of Ccl2 + NeuN double-labeled cells (right) (n = 5, 6).

(D) Representative images (left) and quantification (right) of Foxp3 immunoreactivity in NAc (n = 6); scale bars, 25 μm.

(E) ELISA analysis of IFN-γ in NAc (n = 6).

(F) Representative co-immunostaining images for Stat1, NeuN, and DAPI in Nac; scale bars, 25 μm (left). The percentage of Stat1 + NeuN double-labeled cells (right) (n = 5, 6).

(G–I) The effects of *Ccr2*^{cKO} on morphine-mediated synaptic morphology in NAc by Golgi-Cox staining and TEM.

(G) Histograms showing the distribution of different spine types.

(H) The proportions of stubby-like (left) and thin-like (right) spines (n = 6).

(I) The lengths of active zones in asymmetrical synapses (n = 5).

(J) The effects of *Ccr2*^{cKO} on the global withdrawal score 48 h after the last morphine treatment (n = 6, 7, 8).

Data are shown as the mean ± SEM. Data represent three independent experiments. *p < 0.05, **p < 0.01, ***p < 0.001, ****p < 0.0001 compared with saline group or saline × *Ccr2*^{loxp} group; $^{\#}$p < 0.05, $^{\#\#}$p < 0.01, $^{\#\#\#}$p < 0.001, $^{\#\#\#\#}$p < 0.0001.

See also Figure S7.

We then determined the potential mechanisms of these DEGs of interest in the context of peripheral Treg infiltration-induced NAc synaptic weakening. There is a clear correlation between fatty-acid-binding protein 7 (Fabp7) expression and the level of IFN-γ (Figures 6B and S7M). Strong evidence supports that Fabp7, a differentiation- and migration-associated molecule, modulates BBB permeability.[26] We therefore hypothesized that morphine-induced dysfunction of BBB contributes to Treg infiltration into NAc, which is related to Fabp7 expression. We detected co-localization of Fabp7 with specific cell-type markers (NeuN, neuron; GFAP, astrocyte; and IBA1, microglia) by immunohistochemical analysis. The Fabp7 was particularly highly expressed by astrocytes (approximately 70% of cells), whereas <10% of neurons and microglia were Fabp7^{+} (Figure 6C).

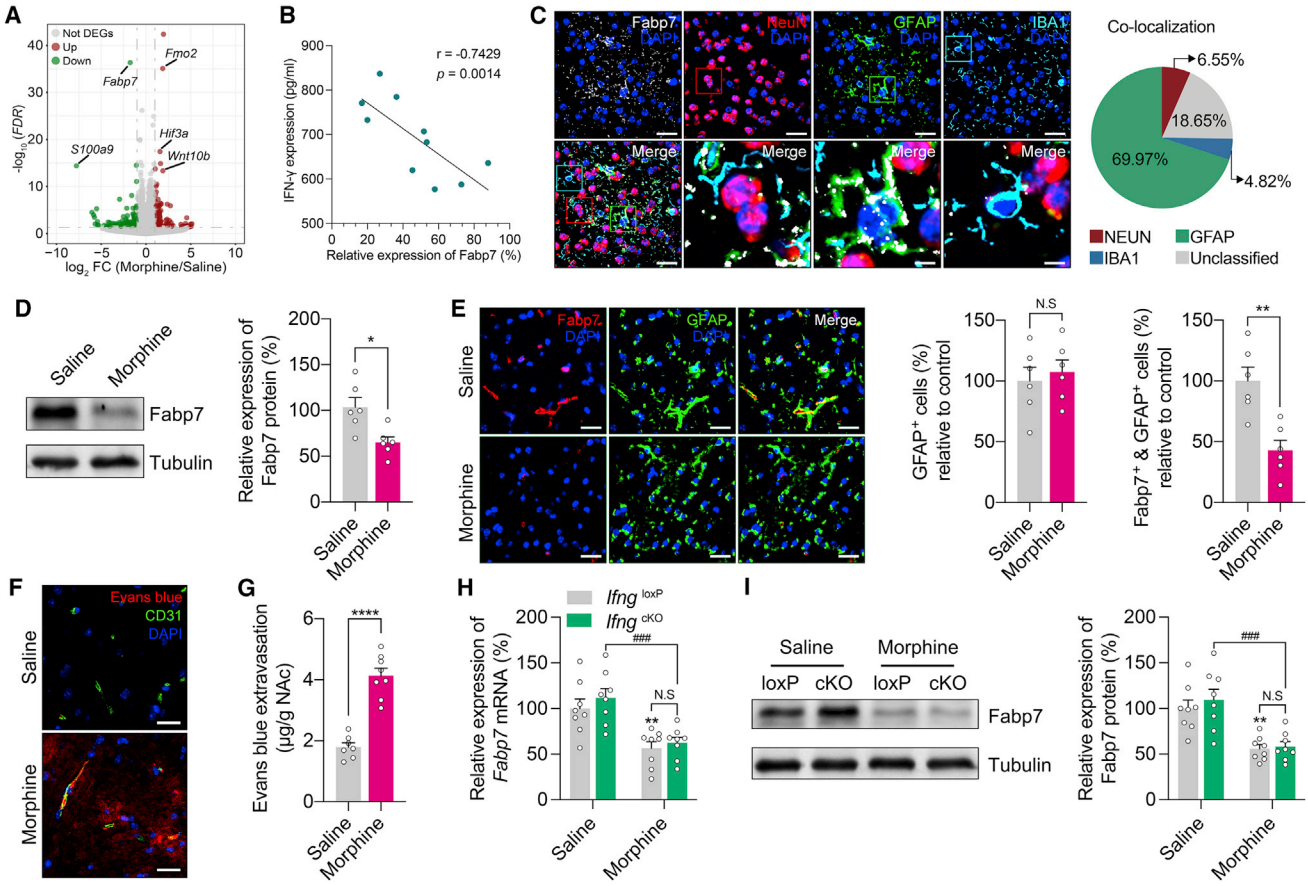


Figure 6. Morphine triggers Fabp7 reduction and BBB hyperpermeability

(A) Bulk RNA-seq showing the gene expression profiles in NAc. The red dots represent significantly upregulated DEGs (n = 111), and the green dots represent significantly downregulated genes (n = 137) (n = 6).

(B) Pearson's correlation analysis between the relative expression of *Fabp7* mRNA and IFN-γ level in NAc (n = 10).

(C) Representative co-immunostaining images for Fabp7, NeuN, GFAP, and IBA1 in NAc (left). The proportion of Fabp7-positive cells contained with NeuN, GFAP, or IBA1 (right). n = 1,099 cells from 4 mice; scale bar (low magnification), 25 μm and (high magnification), 5 μm.

(D and E) The Fabp7 expression in NAc astrocytes.

(D) Representative images of immunoblots (left). The relative protein level of Fabp7 (right) (n = 6).

(E) Representative co-immunostaining images for Fabp7, GFAP, and DAPI; scale bars, 25 μm (left). Quantification of Fabp7 and GFAP immunoreactivity in NAc (right) (n = 6).

(F and G) Extravagated Evans blue (EB) analysis showing the BBB permeability.

(F) Representative fluorescent images for EB; vascular endothelial cells were marked by anti-CD31; scale bars, 25 μm.

(G) Spectrophotometric analysis of EB extravasation in NAc (n = 7, 8).

(H and I) The effects of *Ifng*^{cKO} on Fabp7 expression determined by qPCR and western blotting.

(H) The relative expression of *Fabp7* mRNA (n = 8).

(I) Representative immunoblots (left). The relative expression of Fabp7 protein (right) (n = 8).

Data are shown as the mean ± SEM. Data represent two to four independent experiments. *p < 0.05, **p < 0.01, ****p < 0.0001 compared with saline group (D, E, and G) or saline × *Ifng*^{loxP} group (H and I); ###p < 0.001.

See also Figure S7 and Table S4.

Furthermore, both total (Figure 6D) and astrocyte-derived Fabp7 (Figure 6E) were significantly decreased in morphine-treated mice. Evans blue (EB) monitoring of extravasation was used to assess the permeability of BBB after morphine exposure. Using CD31 as a marker of vascular endothelial cells, we observed an increase of extravasated EB in the morphine-treated NAc (Figures 6F and 6G). Interestingly, *Ifng*^{cKO} mice also exhibited morphine-induced decreases in *Fabp7* mRNA and protein (Figures 6H and 6I), indicating that decreased Fabp7 is attributable to morphine administration but not to IFN-γ. Taken together, these results provide convergent evidence showing that morphine treatment results in neuron-derived Ccl2 expression and hyperpermeability of the BBB, which are associated with Treg recruitment.

The GFAP-driven tet-on system was used to specifically rescue Fabp7 expression (upregulation) in astrocytes of NAc

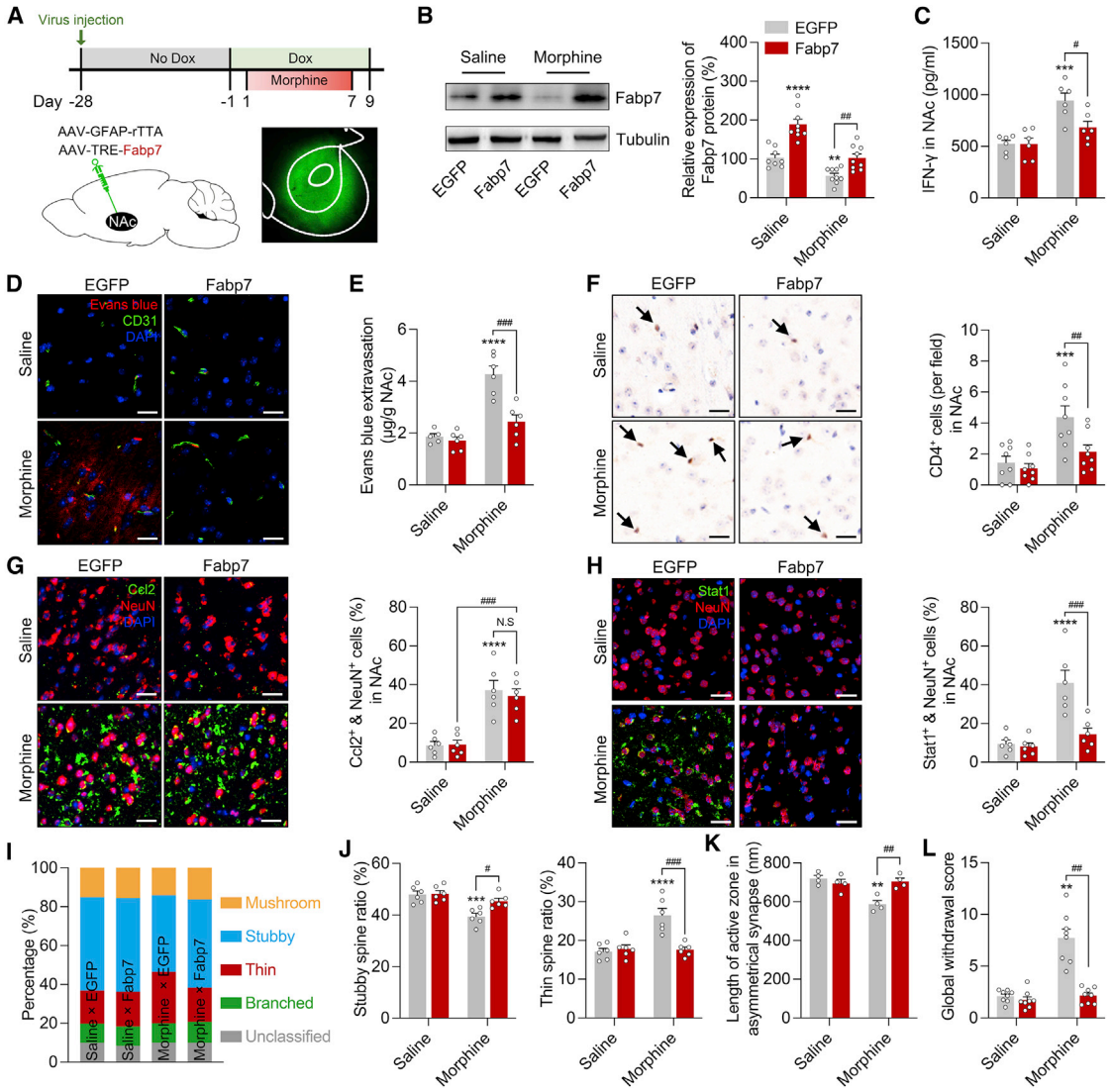


Figure 7. Fabp7 is essential for opioid-associated BBB permeability

(A) The flow chart (upper) and schematic (lower) of the specific overexpression of Fabp7 in NAc astrocytes using a GFAP-driven tet-on system.

(B and C) The efficiency of Fabp7 overexpression in NAc determined by western blotting and ELISA.

(B) Representative images of immunoblots (left). The relative expression of Fabp7 protein (right) (n = 8, 9).

(C) The level of IFN-γ by ELISA in NAc (n = 6).

(D and E) Extravagated EB analysis showing the BBB permeability.

(D) Representative fluorescent images for EB; vascular endothelial cells were marked by anti-CD31; scale bars, 25 μm.

(E) Spectrophotometric analysis of EB extravasation in NAc (n = 5, 6).

(F) Immunohistochemistry showing the Treg infiltration in NAc. Representative $CD4^+$ cells of immunohistochemistry images; scale bars, 25 μm (left). Quantification of $CD4^+$ cells per high-power field (right) (n = 8).

(G) Immunofluorescence showing the Ccl2 expression in NAc neurons. Representative co-immunostaining images for Ccl2, NeuN, and DAPI; scale bars, 25 μm (left). The percentage of Ccl2 + NeuN double-labeled cells (right) (n = 6).

(H) Immunofluorescence showing the Stat1 expression in NAc neurons. Representative co-immunostaining images for Stat1, NeuN, and DAPI; scale bars, 25 μm (left). The percentage of Stat1 + NeuN double-labeled cells (right) (n = 6).

(I–K) The effects of Fabp7 overexpression on synaptic structure of NAc by Golgi-Cox staining and TEM.

(I) Histograms showing the distribution of different spine types.

(J) The proportions of stubby-like (left) and thin-like (right) spines (n = 6).

(K) The lengths of active zones in asymmetrical synapses (n = 4).

(L) The effects of Fabp7 overexpression on the global withdrawal score 48 h after the last morphine treatment (n = 8).

Data are shown as the mean ± SEM. Data represent three to five independent experiments. $^{**}p < 0.01$, $^{***}p < 0.001$, $^{****}p < 0.0001$ compared with saline × EGFP group; $^{\#}p < 0.05$, $^{\#\#}p < 0.01$, $^{\#\#\#}p < 0.001$.

See also Figure S7.

caused by morphine treatment (Figure 7A). Results of qPCR and western blotting confirmed that the injection of the appropriate vector resulted in Fabp7 overexpression in NAc (Figures 7B and S7N). Restoration of Fabp7 significantly reduced the level of IFN-γ in NAc (Figure 7C), while Fabp7 overexpression did not affect morphine-induced IFN-γ expression in blood (Figure S7O). We then investigated the effects of Fabp7 overexpression on BBB permeability and Treg infiltration into NAc and found that this prevented the disruption of the BBB (Figures 7D and 7E) and Treg infiltration (Figure 7F) induced by morphine. Immunofluorescence staining demonstrated that restoration of Fabp7 expression in astrocytes did not reduce MSN-derived Ccl2 production (Figure 7G), suggesting that the elevated Ccl2 was attributable to morphine treatment rather than to Treg infiltration. In contrast, restoration of BBB integrity did reduce morphine-mediated Stat1 expression, resulting in less IFN-γ signaling (Figure 7H). We also determined whether Fabp7 contributes to morphine-induced synaptic changes and withdrawal symptoms. As expected, overexpression of Fabp7 in morphine-treated mice resulted in similar morphology (Figures 7I–7K and S7P–S7S) and withdrawal symptoms (Figures 7L and S7T) compared with saline-treated mice as described above. This suggests that Fabp7 upregulation rescues synaptic weakening and ameliorates withdrawal symptoms after morphine treatment.

DISCUSSION

Our results identified markedly enhanced Foxp3 and CTLA4 expression in opioid-associated blood cells. Interestingly, increased Foxp3^{high} cells were found not only within the CD4$^+$ subset but also in various other immune cells. However, the function of Foxp3 in other cells remains unclear. Unlike classical inhibitory Foxp3$^+$ cells, the opioid-associated Foxp3^{high} cells were characteristically naive (CCR7$^+$ and CD45RA$^+$), mononuclear (CD163$^+$), and activated (Ki67$^+$, ICOS$^+$, OX40$^+$). These findings are consistent with the previous observation that a significant increase in the percentage of Tregs is found in the peripheral blood of patients with opioid use disorder.[27] Opioid drugs are powerful inducers of euphoria and cause severe withdrawal symptoms. Opioid-induced respiratory depression and hypoxia are very common and severe.[9–11] We found a trend toward an increase in Tregs expressing fragile markers, including IFN-γ and HIF1α in blood from patients with opioid use disorder, in response to opioid-induced global hypoxia, confirming that hypoxia condition facilitates Treg fragility that can be present not only in the tumor microenvironment.

The positive correlation between Treg fragility and withdrawal score implies that fragile-like Tregs are involved in mediating withdrawal symptoms. Despite being ''immune privileged,'' the CNS may interact with the immune system to maintain homeostatic immune surveillance. Accumulating evidence suggests that the adaptive immune system affects the brain and behavior in physiological and pathological states.[16,28,29] It is readily apparent that T cells infiltrate into the CNS to correct brain function and recovery after injury. Although a recent study has supported the notion that morphine induces naive splenocyte trafficking into CNS, the mechanism and function of lymphocyte infiltration are not entirely clear.[30] In the present study, synapse-weakening effects were prevented and stable morphological structures retained when IFN-γ or the IFN-γ receptor was decreased. It is intriguing that IFN-γ, response to neurons but not glia, regulates neural activity and social behavior.[31] The role of immune molecules has been previously shown to control brain development and function,[32–34] and a role for cytokines in influencing behavior has been proposed, primarily in the context of sickness behavior and pain,[35,36] which are the major components of withdrawal symptoms. Our data suggest that IFN-γ regulates opioid-induced NAc morphological reconfiguration and withdrawal symptoms.

Our results document that fragile-like Treg trafficking into NAc can be attributed to Ccl2-mediated recruitment and BBB hyperpermeability. Ccl2, already identified as a potential candidate chemokine for Treg trafficking into CNS,[18] is known to be released from neurons after morphine stimulation.[21] We found that morphine administration increased MSN-derived Ccl2 expression, which led to chemotactic effects for fragile-like Tregs in NAc. Fabp7, which is mainly expressed by astrocytes and neural progenitors, preferentially binds to brain-type fatty acids.[37,38] Although emerging evidence has implicated Fabp7 as an essential biological regulator of astrocyte function, several aspects of this activity remain unknown.[39,40] Indeed, our findings demonstrate that astrocyte-derived Fabp7 protects the integrity of the BBB. The caveolin-1/matrix metalloproteinase signaling pathway may be part of the underlying mechanism through which Fabp7 protects the BBB, as previously reported.[26] Interestingly, earlier studies indicated that astrocytic Fabp7 is crucial for dendritic-arbor growth, neuronal excitatory synapse formation, and synaptic transmission.[41] The present study, as mentioned above, confirmed that Fabp7, serving as a key ''switch'' for BBB permeability, represents an endogenous regulator of synaptic plasticity. Moreover, this phenomenon is mainly caused by infiltrating fragile-like Treg-secreted IFN-γ rather than the direct effect of Fabp7.

In summary, our work reveals the landscape of the peripheral immune milieu in patients with opioid use disorder. The impact of the adaptive immune system on CNS has been emphasized here, and our work implies that peripheral blood-derived fragile-like Tregs, triggered by opioid-induced hypoxia, produce IFN-γ and infiltrate into NAc to reshape synaptic plasticity, which regulates withdrawal symptoms. Opioid stimulation not only increases MSN-derived Ccl2 but also represses astrocyte-derived Fabp7, which boosts the entry of fragile-like Tregs into the CNS and thereby contributes to structural and behavioral changes. Our work illustrates the mechanism responsible for the transport of fragile-like Tregs across the BBB and provides insights into the role of the IFN-γ-signaling pathway in modulating the structure and function of MSNs. This ''BBB permeability/fragile-like Treg infiltration/IFN-γ signaling/withdrawal symptom'' axis may provide opportunities leading to the development of an effective immunotherapeutic strategy for opioid-dependent patients.

Limitations of the study

In this work, we identified an expansion of fragile-like Tregs in the blood of patients with opioid use disorder. Several studies have previously indicated an increased level of CD4$^+$ Tregs in opioid abusers.[27,42] However, the molecular mechanism of Treg expansion and the crosstalk between Tregs and other immune cells

remains enigmatic. Considering the localization of Foxp3 to the X-chromosome, $Foxp3^{YFP\text{-}cre}$ mice also should be used as a control due to the Cre effects. Although hypoxia is a critical mechanism to trigger Treg fragility, the difference between opioid-associated fragile-like Tregs and fragile Tregs described in cancer remains largely unknown. Still needed is more functional evidence to test Treg fragility in future work. Although the present study demonstrated that *Wnt10b* is inhibited and synaptic weakening is prevented when IFN-γ signaling is blocked under morphine exposure, the mechanism of synaptic remodeling is very complex. Future work will be needed to fully elucidate how the IFN-γ-signaling pathway influences synaptic connectivity in response to opioid stimuli.

STAR★METHODS

Detailed methods are provided in the online version of this paper and include the following:

- KEY RESOURCES TABLE
- RESOURCE AVAILABILITY
  - Lead contact
  - Materials availability
  - Data and code availability
- EXPERIMENTAL MODEL AND SUBJECT DETAILS
  - Subjects
  - Animals
- METHOD DETAILS
  - Morphine and heroin treatments
  - Mass cytometer (CyTOF) and data analysis
  - Enzyme-linked immunosorbent assay (ELISA)
  - Tissue dissociation and flow cytometry
  - In vitro assays
  - Noninvasive arterial oxygen saturation (SaO_2) measurement
  - TCR IR sequencing and analysis
  - Bulk RNA sequencing and gene expression analysis
  - Spine morphology analysis
  - Analysis of the synaptic ultrastructure
  - RNA isolation and qPCR
  - Immunoblotting
  - Immunohistochemistry
  - Analysis of the permeability of the BBB
  - Stereotaxic injections
  - Conditioned place preference (CPP)
  - Spontaneous morphine withdrawal monitoring
- QUANTIFICATION AND STATISTICAL ANALYSIS

SUPPLEMENTAL INFORMATION

Supplemental information can be found online at https://doi.org/10.1016/j.cell.2022.12.030.

ACKNOWLEDGMENTS

This work was supported by the National Natural Science Foundation of China (82171878, 81900569, 82000592, and 82001999), the Natural Science Foundation of Fujian Province (2021J01017 and 2022J01011), the Fundamental Research Funds for the Central Universities (20720190080), and the Natural Science Foundation of Shaanxi Province (2021JM-028). We are grateful to Professor Guo Fu, Changchun Xiao, Zhihai Peng, and Juan Lin (Xiamen University) for assisting. The authors would like to thank Shaan Probiomicros Co., Ltd. (Xi'an, China), MUSI biotech Co., Ltd. (Shanghai, China), and PUCG biotech Co., Ltd. (Shanghai, China) for technical support.

AUTHOR CONTRIBUTIONS

Kejia Wang and Y.Z. conceived and designed the study; R.W., J.L., H.T., X.B., P.Y., Q.L., F.Z., Kena Wang, Y.L., J.D., R.Z., W.D., B.Z., Q.F., Q.Z., and C.K. performed the experiments; X.X. and R.Y. analyzed the CyTOF data; Y.C. and C.Z. analyzed the bulk RNA-seq data; X.C. and P.Y. analyzed the bulk IR-seq data; and Kejia Wang and Y.Z. wrote the manuscript.

DECLARATION OF INTERESTS

The authors declare no conflicting interests.

Received: February 1, 2022
Revised: September 4, 2022
Accepted: December 19, 2022
Published: January 19, 2023

REFERENCES

1. Lammel, S., Ion, D.I., Roeper, J., and Malenka, R.C. (2011). Projection-specific modulation of dopamine neuron synapses by aversive and rewarding stimuli. Neuron *70*, 855–862. https://doi.org/10.1016/j.neuron.2011.03.025.
2. Salgado, S., and Kaplitt, M.G. (2015). The nucleus accumbens: a comprehensive review. Stereotact. Funct. Neurosurg. *93*, 75–93. https://doi.org/10.1159/000368279.
3. Alcantara, A.A., Lim, H.Y., Floyd, C.E., Garces, J., Mendenhall, J.M., Lyons, C.L., and Berlanga, M.L. (2011). Cocaine- and morphine-induced synaptic plasticity in the nucleus accumbens. Synapse *65*, 309–320. https://doi.org/10.1002/syn.20849.
4. Yong, Z., Yan, L., Gao, X., Gong, Z., and Su, R. (2014). Effects of Thienorphine on synaptic structure and synaptophysin expression in the rat nucleus accumbens. Neuroscience *274*, 53–58. https://doi.org/10.1016/j.neuroscience.2014.05.026.
5. Cahill, M.E., Browne, C.J., Wang, J.S., Hamilton, P.J., Dong, Y., and Nestler, E.J. (2018). Withdrawal from repeated morphine administration augments expression of the RhoA network in the nucleus accumbens to control synaptic structure. J. Neurochem. *147*, 84–98. https://doi.org/10.1111/jnc.14563.
6. Pimentel, E., Sivalingam, K., Doke, M., and Samikkannu, T. (2020). Effects of drugs of abuse on the blood-brain barrier: a brief overview. Front. Neurosci. *14*, 513. https://doi.org/10.3389/fnins.2020.00513.
7. Overacre-Delgoffe, A.E., Chikina, M., Dadey, R.E., Yano, H., Brunazzi, E.A., Shayan, G., Horne, W., Moskovitz, J.M., Kolls, J.K., Sander, C., et al. (2017). Interferon-gamma drives Treg fragility to promote anti-tumor immunity. Cell *169*, 1130–1141.e11. https://doi.org/10.1016/j.cell.2017.05.005.
8. Overacre-Delgoffe, A.E., and Vignali, D.A.A. (2018). Treg fragility: A prerequisite for effective antitumor immunity? Cancer Immunol. Res. *6*, 882–887. https://doi.org/10.1158/2326-6066.CIR-18-0066.
9. Boom, M., Niesters, M., Sarton, E., Aarts, L., Smith, T.W., and Dahan, A. (2012). Non-analgesic effects of opioids: opioid-induced respiratory depression. Curr. Pharm. Des. *18*, 5994–6004. https://doi.org/10.2174/138161212803582469.
10. Kiyatkin, E.A. (2019). Respiratory depression and brain hypoxia induced by opioid drugs: morphine, oxycodone, heroin, and fentanyl. Neuropharmacology *151*, 219–226. https://doi.org/10.1016/j.neuropharm.2019.02.008.

11. Algera, M.H., Kamp, J., van der Schrier, R., van Velzen, M., Niesters, M., Aarts, L., Dahan, A., and Olofsen, E. (2019). Opioid-induced respiratory depression in humans: a review of pharmacokinetic-pharmacodynamic modelling of reversal. Br. J. Anaesth. *122*, e168–e179. https://doi.org/10.1016/j.bja.2018.12.023.

12. Robins, H.S., Campregher, P.V., Srivastava, S.K., Wacher, A., Turtle, C.J., Kahsai, O., Riddell, S.R., Warren, E.H., and Carlson, C.S. (2009). Comprehensive assessment of T-cell receptor beta-chain diversity in alphabeta T cells. Blood *114*, 4099–4107. https://doi.org/10.1182/blood-2009-04-217604.

13. Graziane, N.M., Sun, S., Wright, W.J., Jang, D., Liu, Z., Huang, Y.H., Nestler, E.J., Wang, Y.T., Schlüter, O.M., and Dong, Y. (2016). Opposing mechanisms mediate morphine- and cocaine-induced generation of silent synapses. Nat. Neurosci. *19*, 915–925. https://doi.org/10.1038/nn.4313.

14. Bello-Medina, P.C., Flores, G., Quirarte, G.L., McGaugh, J.L., and Prado Alcalá, R.A. (2016). Mushroom spine dynamics in medium spiny neurons of dorsal striatum associated with memory of moderate and intense training. Proc. Natl. Acad. Sci. USA *113*, E6516–E6525. https://doi.org/10.1073/pnas.1613680113.

15. Zhu, Y., Wienecke, C.F., Nachtrab, G., and Chen, X. (2016). A thalamic input to the nucleus accumbens mediates opiate dependence. Nature *530*, 219–222. https://doi.org/10.1038/nature16954.

16. Dulken, B.W., Buckley, M.T., Navarro Negredo, P., Saligrama, N., Cayrol, R., Leeman, D.S., George, B.M., Boutet, S.C., Hebestreit, K., Pluvinage, J.V., et al. (2019). Single-cell analysis reveals T cell infiltration in old neurogenic niches. Nature *571*, 205–210. https://doi.org/10.1038/s41586-019-1362-5.

17. Teo, S., and Salinas, P.C. (2021). Wnt-frizzled signaling regulates activity-mediated synapse formation. Front. Mol. Neurosci. *14*, 683035. https://doi.org/10.3389/fnmol.2021.683035.

18. Chang, A.L., Miska, J., Wainwright, D.A., Dey, M., Rivetta, C.V., Yu, D., Kanojia, D., Pituch, K.C., Qiao, J., Pytel, P., et al. (2016). CCL2 produced by the glioma microenvironment is essential for the recruitment of regulatory t cells and myeloid-derived suppressor cells. Cancer Res. *76*, 5671–5682. https://doi.org/10.1158/0008-5472.CAN-16-0144.

19. Förster, R., Davalos-Misslitz, A.C., and Rot, A. (2008). CCR7 and its ligands: balancing immunity and tolerance. Nat. Rev. Immunol. *8*, 362–371. https://doi.org/10.1038/nri2297.

20. Di Liberto, G., Pantelyushin, S., Kreutzfeldt, M., Page, N., Musardo, S., Coras, R., Steinbach, K., Vincenti, I., Klimek, B., Lingner, T., et al. (2018). Neurons under T cell attack coordinate phagocyte-mediated synaptic stripping. Cell *175*, 458–471.e19. e419. https://doi.org/10.1016/j.cell.2018.07.049.

21. Rock, R.B., Hu, S., Sheng, W.S., and Peterson, P.K. (2006). Morphine stimulates CCL2 production by human neurons. J. Neuroinflammation *3*, 32. https://doi.org/10.1186/1742-2094-3-32.

22. Chaudhary, H., Iashchishyn, I.A., Romanova, N.V., Rambaran, M.A., Musteikyte, G., Smirnovas, V., Holmboe, M., Ohlin, C.A., Svedružić, Ž.M., and Morozova-Roche, L.A. (2021). Polyoxometalates as effective nano-inhibitors of amyloid aggregation of pro-inflammatory S100A9 protein involved in neurodegenerative diseases. ACS Appl. Mater. Interfaces *13*, 26721–26734. https://doi.org/10.1021/acsami.1c04163.

23. Dasgupta, M., Shashikanth, M., Gupta, A., Sandhu, A., De, A., Javed, S., and Singh, V. (2020). NHR-49 transcription factor regulates immunometabolic response and survival of Caenorhabditis elegans during Enterococcus faecalis infection. Infect. Immun. *88*, e00130-20. https://doi.org/10.1128/IAI.00130-20.

24. Kumar, H., Lim, J.H., Kim, I.S., and Choi, D.K. (2015). Differential regulation of HIF-3α in LPS-induced BV-2 microglial cells: comparison and characterization with HIF-1α. Brain Res. *1610*, 33–41. https://doi.org/10.1016/j.brainres.2015.03.046.

25. Lüscher, C., and Malenka, R.C. (2011). Drug-evoked synaptic plasticity in addiction: from molecular changes to circuit remodeling. Neuron *69*, 650–663. https://doi.org/10.1016/j.neuron.2011.01.017.

26. Rui, Q., Ni, H., Lin, X., Zhu, X., Li, D., Liu, H., and Chen, G. (2019). Astrocyte-derived fatty acid-binding protein 7 protects blood-brain barrier integrity through a caveolin-1/MMP signaling pathway following traumatic brain injury. Exp. Neurol. *322*, 113044. https://doi.org/10.1016/j.expneurol.2019.113044.

27. Riss, G.L., Chang, D.I., Wevers, C., Westendorf, A.M., Buer, J., Scherbaum, N., and Hansen, W. (2012). Opioid maintenance therapy restores CD4+ T cell function by normalizing CD4+CD25(high) regulatory T cell frequencies in heroin user. Brain Behav. Immun. *26*, 972–978. https://doi.org/10.1016/j.bbi.2012.05.008.

28. Ribeiro, M., Brigas, H.C., Temido-Ferreira, M., Pousinha, P.A., Regen, T., Santa, C., Coelho, J.E., Marques-Morgado, I., Valente, C.A., Omenetti, S., et al. (2019). Meningeal γδ T cell-derived IL-17 controls synaptic plasticity and short-term memory. Sci. Immunol. *4*, eaay5199. https://doi.org/10.1126/sciimmunol.aay5199.

29. Filiano, A.J., Gadani, S.P., and Kipnis, J. (2017). How and why do T cells and their derived cytokines affect the injured and healthy brain? Nat. Rev. Neurosci. *18*, 375–384. https://doi.org/10.1038/nrn.2017.39.

30. Olin, M., Oh, S., Roy, S., Peterson, P., and Molitor, T. (2012). Morphine induces splenocyte trafficking into the CNS. J. Neuroimmune Pharmacol. *7*, 436–443. https://doi.org/10.1007/s11481-011-9307-2.

31. Filiano, A.J., Xu, Y., Tustison, N.J., Marsh, R.L., Baker, W., Smirnov, I., Overall, C.C., Gadani, S.P., Turner, S.D., Weng, Z.P., et al. (2016). Unexpected role of interferon-gamma in regulating neuronal connectivity and social behaviour. Nature *535*, 425–429. https://doi.org/10.1038/nature18626.

32. Datwani, A., McConnell, M.J., Kanold, P.O., Micheva, K.D., Busse, B., Shamloo, M., Smith, S.J., and Shatz, C.J. (2009). Classical MHCI molecules regulate retinogeniculate refinement and limit ocular dominance plasticity. Neuron *64*, 463–470. https://doi.org/10.1016/j.neuron.2009.10.015.

33. Djurisic, M., Vidal, G.S., Mann, M., Aharon, A., Kim, T., Ferrao Santos, A.F., Zuo, Y., Hübener, M., and Shatz, C.J. (2013). PirB regulates a structural substrate for cortical plasticity. Proc. Natl. Acad. Sci. USA *110*, 20771–20776. https://doi.org/10.1073/pnas.1321092110.

34. Monteiro, S., Roque, S., Marques, F., Correia-Neves, M., and Cerqueira, J.J. (2017). Brain interference: revisiting the role of IFNγ in the central nervous system. Prog. Neurobiol. *156*, 149–163. https://doi.org/10.1016/j.pneurobio.2017.05.003.

35. McCusker, R.H., and Kelley, K.W. (2013). Immune-neural connections: how the immune system's response to infectious agents influences behavior. J. Exp. Biol. *216*, 84–98. https://doi.org/10.1242/jeb.073411.

36. Scholz, J., and Woolf, C.J. (2007). The neuropathic pain triad: neurons, immune cells and glia. Nat. Neurosci. *10*, 1361–1368. https://doi.org/10.1038/nn1992.

37. Gerstner, J.R., Perron, I.J., Riedy, S.M., Yoshikawa, T., Kadotani, H., Owada, Y., Van Dongen, H.P.A., Galante, R.J., Dickinson, K., Yin, J.C.P., et al. (2017). Normal sleep requires the astrocyte brain-type fatty acid binding protein FABP7. Sci. Adv. *3*, e1602663. https://doi.org/10.1126/sciadv.1602663.

38. Smathers, R.L., and Petersen, D.R. (2011). The human fatty acid-binding protein family: evolutionary divergences and functions. Hum. Genomics *5*, 170–191. https://doi.org/10.1186/1479-7364-5-3-170.

39. Islam, A., Kagawa, Y., Miyazaki, H., Shil, S.K., Umaru, B.A., Yasumoto, Y., Yamamoto, Y., and Owada, Y. (2019). FABP7 protects astrocytes against ROS Toxicity via lipid droplet formation. Mol. Neurobiol. *56*, 5763–5779. https://doi.org/10.1007/s12035-019-1489-2.

40. Killoy, K.M., Harlan, B.A., Pehar, M., and Vargas, M.R. (2020). FABP7 upregulation induces a neurotoxic phenotype in astrocytes. Glia *68*, 2693–2704. https://doi.org/10.1002/glia.23879.

41. Ebrahimi, M., Yamamoto, Y., Sharifi, K., Kida, H., Kagawa, Y., Yasumoto, Y., Islam, A., Miyazaki, H., Shimamoto, C., Maekawa, M., et al. (2016). Astrocyte-expressed FABP7 regulates dendritic morphology and

excitatory synaptic function of cortical neurons. Glia *64*, 48–62. https://doi.org/10.1002/glia.22902.

42. Hansen, W., Luppus, S., Barthel, R., Chang, D.I., Broemstrup, J., Zwarg, T., Shibata, J., Westendorf, A.M., Buer, J., and Scherbaum, N. (2021). Heroin-assisted treatment of heroin-addicted patients normalizes regulatory T cells but does not restore $CD4^+$ T cell proliferation. Addict. Biol. *26*, e12998. https://doi.org/10.1111/adb.12998.
43. Love, M.I., Huber, W., and Anders, S. (2014). Moderated estimation of fold change and dispersion for RNA-seq data with DESeq2. Genome Biol. *15*, 550. https://doi.org/10.1186/s13059-014-0550-8.
44. Yu, G., Wang, L.G., Han, Y., and He, Q.Y. (2012). clusterProfiler: an R package for comparing biological themes among gene clusters. Omics *16*, 284–287. https://doi.org/10.1089/omi.2011.0118.
45. Van Gassen, S., Callebaut, B., Van Helden, M.J., Lambrecht, B.N., Demeester, P., Dhaene, T., and Saeys, Y. (2015). FlowSOM: using self-organizing maps for visualization and interpretation of cytometry data. Cytometry A *87*, 636–645. https://doi.org/10.1002/cyto.a.22625.
46. Levine, J.H., Simonds, E.F., Bendall, S.C., Davis, K.L., Amir, el-A.D., Tadmor, M.D., Litvin, O., Fienberg, H.G., Jager, A., Zunder, E.R., et al. (2015). Data-driven phenotypic dissection of AML reveals progenitor-like cells that correlate with prognosis. Cell *162*, 184–197. https://doi.org/10.1016/j.cell.2015.05.047.
47. Sun, H.Q., Bao, Y.P., Zhou, S.J., Meng, S.Q., and Lu, L. (2014). The new pattern of drug abuse in China. Curr. Opin. Psychiatry *27*, 251–255. https://doi.org/10.1097/YCO.0000000000000073.
48. Lutz, P.E., and Kieffer, B.L. (2013). The multiple facets of opioid receptor function: implications for addiction. Curr. Opin. Neurobiol. *23*, 473–479. https://doi.org/10.1016/j.conb.2013.02.005.
49. Liang, Q., Hu, Y., Zhang, M., Lin, C., Zhang, W., Li, Y., Zhu, P., Xue, P., Chen, Y., Li, Q., et al. (2020). The T cell receptor immune repertoire protects the liver from Reconsitution. Front. Immunol. *11*, 584979. https://doi.org/10.3389/fimmu.2020.584979.
50. Avey, D., Sankararaman, S., Yim, A.K.Y., Barve, R., Milbrandt, J., and Mitra, R.D. (2018). Single-cell RNA-seq uncovers a robust transcriptional response to morphine by glia. Cell Rep. *24*, 3619–3629.e4. https://doi.org/10.1016/j.celrep.2018.08.080.
51. Liang, Q., Liu, Z., Zhu, C., Wang, B., Liu, X., Yang, Y., Lv, X., Mu, H., and Wang, K. (2018). Intrahepatic T-cell receptor beta immune repertoire is essential for liver regeneration. Hepatology *68*, 1977–1990. https://doi.org/10.1002/hep.30067.
52. Liang, Q., Zhang, M., Hu, Y., Zhang, W., Zhu, P., Chen, Y., Xue, P., Li, Q., and Wang, K. (2020). Gut microbiome contributes to liver fibrosis impact on T cell receptor immune repertoire. Front. Microbiol. *11*, 571847. https://doi.org/10.3389/fmicb.2020.571847.
53. Risher, W.C., Ustunkaya, T., Singh Alvarado, J., and Eroglu, C. (2014). Rapid Golgi analysis method for efficient and unbiased classification of dendritic spines. PLoS One *9*, e107591. https://doi.org/10.1371/journal.pone.0107591.
54. Craig, E., Dillingham, C.M., Milczarek, M.M., Phillips, H.M., Davies, M., Perry, J.C., and Vann, S.D. (2020). Lack of change in CA1 dendritic spine density or clustering in rats following training on a radial-arm maze task. Wellcome Open Res. *5*, 68. https://doi.org/10.12688/wellcomeopenres.15745.2.
55. Qu, W., and Li, L. (2020). Loss of TREM2 confers resilience to synaptic and cognitive impairment in aged mice. J. Neurosci. *40*, 9552–9563. https://doi.org/10.1523/JNEUROSCI.2193-20.2020.
56. Ball, K.T., Wellman, C.L., Fortenberry, E., and Rebec, G.V. (2009). Sensitizing regimens of (+/-)3, 4-methylenedioxymethamphetamine (Ecstasy) elicit enduring and differential structural alterations in the brain motive circuit of the rat. Neuroscience *160*, 264–274. https://doi.org/10.1016/j.neuroscience.2009.02.025.
57. Yan, P., Xu, D., Ji, Y., Yin, F., Cui, J., Su, R., Wang, Y., Zhu, Y., Wei, S., and Lai, J. (2019). LiCl pretreatment ameliorates adolescent methamphetamine exposure-induced long-term alterations in behavior and hippocampal ultrastructure in adulthood in mice. Int. J. Neuropsychopharmacol. *22*, 303–316. https://doi.org/10.1093/ijnp/pyz001.
58. Pulipparacharuvil, S., Renthal, W., Hale, C.F., Taniguchi, M., Xiao, G., Kumar, A., Russo, S.J., Sikder, D., Dewey, C.M., Davis, M.M., et al. (2008). Cocaine regulates MEF2 to control synaptic and behavioral plasticity. Neuron *59*, 621–633. https://doi.org/10.1016/j.neuron.2008.06.020.
59. Papaleo, F., and Contarino, A. (2006). Gender- and morphine dose-linked expression of spontaneous somatic opiate withdrawal in mice. Behav. Brain Res. *170*, 110–118. https://doi.org/10.1016/j.bbr.2006.02.009.
60. Lu, G., Zhou, Q.X., Kang, S., Li, Q.L., Zhao, L.C., Chen, J.D., Sun, J.F., Cao, J., Wang, Y.J., Chen, J., et al. (2010). Chronic morphine treatment impaired hippocampal long-term potentiation and spatial memory via accumulation of extracellular adenosine acting on adenosine A1 receptors. J. Neurosci. *30*, 5058–5070. https://doi.org/10.1523/JNEUROSCI.0148-10.2010.
61. Papaleo, F., Kitchener, P., and Contarino, A. (2007). Disruption of the CRF/CRF1 receptor stress system exacerbates the somatic signs of opiate withdrawal. Neuron *53*, 577–589. https://doi.org/10.1016/j.neuron.2007.01.022.

STAR★METHODS

KEY RESOURCES TABLE

REAGENT or RESOURCE	SOURCE	IDENTIFIER
Antibodies		
Anti-CD45 (HI30)	BioLegend	Cat# 304002; RRID: AB_314390
Anti-CD3 (UCHT1)	Bio X Cell	Cat# BE0231; RRID: AB_2687713
Anti-CD56 (NCAM16.2)	BD Biosciences	Cat# 559043; RRID: AB_397180
Anti-CD123 (6H6)	BioLegend	Cat# 306002; RRID: AB_314576
Anti-CD274 (29E.2A3)	BioLegend	Cat# 329716; RRID: AB_11149168
Anti-CD14 (M5E2)	BioLegend	Cat# 301862; RRID: AB_2814125
Anti-CD274 (PDL1) (O323)	BioLegend	Cat# 302802; RRID: AB_314294
Anti-CD11a (HI111)	BioLegend	Cat# 301234; RRID: AB_2832577
Anti-CD197 (CCR7) (G043H7)	BioLegend	Cat# 353256; RRID: AB_2814291
Anti-CD19 (HIB19)	BioLegend	Cat# 302268; RRID: AB_2832580
Anti-CD33 (WM53)	BioLegend	Cat# 303419; RRID: AB_2562818
Anti-CD223-165Ho-874501 (LAG3)	Fluidigm	Cat# 3165028; RRID: AB_2687859
Anti-CD45RO (UCHL1)	BioLegend	Cat# 304202; RRID: AB_314418
Anti-CD195 (CCR5) (J418F1)	BioLegend	Cat# 359102; RRID: AB_2562457
Anti-CD366 (Tim3) (F38-2E2)	BioLegend	Cat# 345010; RRID: AB_11150780
Anti-T-bet (4B10)	BioLegend	Cat# 644802; RRID: AB_1595503
Anti-CD45RA (HI100)	BioLegend	Cat# 304102; RRID: AB_314406
Anti-CD194 (CCR4) (L291H4)	BioLegend	Cat# 359402; RRID: AB_2562364
Anti-CD206 (MMR) (15-2)	BioLegend	Cat# 321150; RRID: AB_2819952
Anti-CD127 (IL-7R alpha) (A019D5)	BioLegend	Cat# 351302; RRID: AB_10718513
Anti-CD11c (BU15)	BioLegend	Cat# 337202; RRID: AB_1236381
Anti-IL-2r alpha -24212	R and D Systems	Cat# FAB1020P; RRID: AB_356980
Anti-CD152 (CTLA4) (14D3)	Thermo Fisher Scientific	Cat# 14-1529-82; RRID: AB_467512
Anti-Foxp3 (PCH101)	Thermo Fisher Scientific	Cat# 14-4776-82; RRID: AB_467554
Anti-CD163 (GHI/61)	BioLegend	Cat# 333602; RRID: AB_1088991
Anti-CD38 (HIT2)	BioLegend	Cat# 303502; RRID: AB_314354
Anti-CD44 (BJ18)	BioLegend	Cat# 338802; RRID: AB_1501199
Anti-CD69 (FN50)	BioLegend	Cat# 310902; RRID: AB_314837
Anti-CD36 (5-271)	BioLegend	Cat# 336202; RRID: AB_1279228
Anti-CD137 (4-1BB) (4B4-1)	BioLegend	Cat# 309802; RRID: AB_314781
Anti-Ki67 (SolA15)	Thermo Fisher Scientific	Cat# 14-5698-82; RRID: AB_10854564
Anti-CD7 (CD7-6B7)	BioLegend	Cat# 343102; RRID: AB_1659214
Anti-CD279 (PD1) (EH12.2H7)	BioLegend	Cat# 329926; RRID: AB_11147365
Anti-CD273 (B7-DC, PDL2) (24F.10C12)	BioLegend	Cat# 329610; RRID: AB_1089023
Anti-CD278 (ICOS) (C398.4A)	BioLegend	Cat# 313502; RRID: AB_416326
Anti-CD134 (OX40) (BER-ACT35)	BioLegend	Cat# 350002; RRID: AB_10639951
Anti-CD16 (3G8)	BioLegend	Cat# 302050; RRID: AB_2561481
Anti-HLA-DR (L243)	BioLegend	Cat# 307648; RRID: AB_2561493
Anti-CD4 (RPA-T4)	BioLegend	Cat# 300570; RRID: AB_2810427
Anti-CD8a (RPA-T8)	BioLegend	Cat# 301074; RRID: AB_2814117
Anti-CD11b (M1/70)	BioLegend	Cat# 101202; RRID: AB_312785
Anti-Hif1α	Solarbio	Cat# K000450P; RRID: AB_2922439
Anti-phospho-Akt (Ser473)	Solarbio	Cat# K009354P; RRID: AB_2922440
Anti-pan Akt	Solarbio	Cat# K106557P; RRID: AB_2922441

(*Continued on next page*)

Continued

REAGENT or RESOURCE	SOURCE	IDENTIFIER
Anti-Foxo3a	Solarbio	Cat# K001577P; RRID: AB_2922442
Anti-Foxo1	Solarbio	Cat# K007489P; RRID: AB_2922443
Anti-Fabp7	Abcam	Cat# ab32423; RRID: AB_880078
Anti-Ifngr1	Servicebio	Cat# GB113635; RRID: AB_2922438
Anti-Rip3 (E7A7F)	Cell Signaling Technology	Cat# 10188; RRID: AB_2904619
Anti-phospho-Rip3 (S232) (EPR9516(N)-25)	Abcam	Cat# ab195117; RRID: AB_2768156
Anti-β-Tubulin (9F3)	Cell Signaling Technology	Cat# 2128; RRID: AB_823664
Anti-CD4 (EPR19514)	Abcam	Cat# ab183685; RRID: AB_2686917
Anti-Foxp3	Servicebio	Cat# GB112325, RRID: AB_2922969
Anti-CD19	Servicebio	Cat# GB11061-1; RRID: AB_2922437
Anti-NK1.1 (EPR21236)	Abcam	Cat# ab234107; RRID: AB_2922430
Anti-Ly6c (ER-MP20)	Abcam	Cat# ab54223; RRID: AB_881384
Anti-NeuN (E4M5P)	Cell Signaling Technology	Cat# 94403; RRID: AB_2904530
Anti-NeuN	Servicebio	Cat# GB11138; RRID: AB_2868432
Anti-CD31	Servicebio	Cat# GB11063-2; RRID: AB_2922436
Anti-Ccl2	Servicebio	Cat# GB11199; RRID: AB_2922435
Anti-Stat1 (1F7C6)	Proteintech	Cat# 66545; RRID: AB_2881907
Anti-c-Fos (2H2)	Abcam	Cat# ab208942; RRID: AB_2747772
Anti-GFAP	Servicebio	Cat# GB12096; RRID: AB_2922432
Anti-IBA1	Servicebio	Cat# GB12105; RRID: AB_2922434
InVivoPlus anti-IFNγ (XMG1.2)	Bio X Cell	Cat# BE0055; RRID: AB_1107694
PE anti-Foxp3 (150D)	BioLegend	Cat# 320007; RRID: AB_492981
FITC anti-CD4 (A161A1)	BioLegend	Cat# 357406; RRID: AB_2562357
APC anti-IFNγ (4S.B3)	BioLegend	Cat# 502512; RRID: AB_315237
APC anti-IFNγ (XMG1.2)	BioLegend	Cat# 505810; RRID: AB_315404
APC anti-IFNγR β chain (MOB-47)	BioLegend	Cat# 113606; RRID: AB_2783052
APC anti-T-bet (4B10)	BioLegend	Cat# 644814; RRID: AB_10901173
PE anti-CD8a (53-6.7)	BioLegend	Cat# 100708; RRID: AB_312747
FITC anti-CD4 (GK1.5)	BioLegend	Cat# 100406; RRID: AB_312691
PerCP anti-CD3 (HIT3a)	BioLegend	Cat# 300326; RRID: AB_2616610
PE anti-CD7 (4H9/CD7)	BioLegend	Cat# 395603; RRID: AB_2820048
PE anti-CD8a (HIT8a)	BioLegend	Cat# 300908; RRID: AB_314112
PE anti-CD11a (HI111)	BioLegend	Cat# 301208; RRID: AB_314146
FITC anti-CD19 (HIB19)	BioLegend	Cat# 302205; RRID: AB_314235
FITC anti-CD44 (IM7)	BioLegend	Cat# 103022; RRID: AB_493685
FITC anti-CD56 (NCAM) (HCD56)	BioLegend	Cat# 318303; RRID: AB_604091
PE anti-HLA-DR (LN3)	BioLegend	Cat# 327008; RRID: AB_893571
Alexa488-conjugated donkey anti-mouse IgG	Abcam	Cat# ab150105, RRID: AB_2732856
Alexa594-conjugated donkey anti-rabbit IgG	Abcam	Cat# ab150064, RRID: AB_2734146
Alexa647-conjugated donkey anti-mouse IgG	Abcam	Cat# ab150107, RRID: AB_2890037
HRP-conjugated donkey anti-rabbit IgG	Abcam	Cat# ab205722, RRID: AB_2904602
Bacterial and virus strains		
rAAV2/9-TRE-EGFP-scrambled	OBiO Technology	N/A
rAAV2/9-TRE-EGFP-shRNA (Ifngr1)	OBiO Technology	N/A
rAAV2/9-hSyn-rTTA	OBiO Technology	N/A

(*Continued on next page*)

Continued

REAGENT or RESOURCE	SOURCE	IDENTIFIER
rAAV2/9-GFAP-rTTA	Brain VTA Biotechnology	N/A
rAAV2/9-TRE3g-Fabp7-EGFP	Brain VTA Biotechnology	N/A
rAAV2/9-TRE3g-EGFP	Brain VTA Biotechnology	N/A
rAAV2/Retro-hSyn-Cre	Brain VTA Biotechnology	N/A
rAAV2/9-CaMKIIa-DIO-hM4Di-mCherry	Brain VTA Biotechnology	N/A
rAAV2/9-hSyn-hM4Di-mCherry	Brain VTA Biotechnology	N/A
Chemicals, peptides, and recombinant proteins		
Evans Blue	Sigma-Aldrich	Cat# E2129
Fluorogold (FG)	Fluorochrome	N/A
Doxycycline hydrochloride	MedChemExpress	Cat# HY-N0565A
Clozapine N-oxide	Sigma-Aldrich	Cat# C0832
Recombinant Human IL-2	Novoprotein	Cat# C013
Ionomycin	Sigma-Aldrich	Cat# I3909
PMA	Sigma-Aldrich	Cat# P1585
HCL-morphine	The Third Research Institute of The Ministry of Public Security, Shanghai, China	N/A
HCL-heroin	The Third Research Institute of The Ministry of Public Security, Shanghai, China	N/A
Critical commercial assays		
TUNEL Cell Apoptosis Detection Kit	Servicebio	Cat# G1501
Mouse IFN-γ ELISA kit	Sinobestbio	Cat# YX-E21827
Mouse TGF-β ELISA kit	Sinobestbio	Cat# YX-200708M
Mouse IL-6 ELISA kit	Sinobestbio	Cat# YX-E20013
Mouse IL-10 ELISA kit	Sinobestbio	Cat# YX-E20006
Mouse TNF-α ELISA kit	Sinobestbio	Cat# YX-E20221
Mouse Ccl2 ELISA kit	Sinobestbio	Cat# YX-E22099
Mouse Ccl19 ELISA kit	Sinobestbio	Cat# YX-E20201
Mouse Ccl21ELISA kit	Sinobestbio	Cat# YX-E22082
Mouse IL-17 ELISA kit	Sinobestbio	Cat# YX-E21957
NEBNext® Ultra™ II Directional RNA Library Prep Kit	New England Biolabs	Cat# E7760
Transcriptor First-Strand cDNA Synthesis Kit	Roche Applied Science	Cat# 04896866001
Papain dissociation system	Worthington	Cat# LK003150
Rabbit enhanced polymer detection system	ZSGB-Bio	Cat# PV-9001; RRID: AB_2868452
Rat enhanced polymer detection system	ZSGB-Bio	Cat# PV-9004; RRID: AB_2868453
TSAPLus Fluorescence Triple Staining Kit Tyramide Signal Amplification Immunofluorescence Reagent	Servicebio	Cat# G1236
Deposited data		
Bulk NAc RNA sequencing	This paper	CRA004392; https://ngdc.cncb.ac.cn/gsa
Bulk NAc IR sequencing	This paper	CRA004392; https://ngdc.cncb.ac.cn/gsa
Bulk human PBMCsq RNA sequencing	This paper	HRA002120; https://ngdc.cncb.ac.cn/gsa
Experimental models: Organisms/strains		
Mouse: B6.129(Cg)-*Foxp3*$^{tm4(YFP/icre)Ayr}$	The Jackson Laboratory	RRID: IMSR_JAX:016959
Mouse: C57BL/6J-*Ccr2*$^{em1C(flox)}$	GemPharmatech	Strain# T005892;
Mouse: C57BL/6J-*Ifng*$^{em1C(flox)}$	Cyagen Biosciences	Cat# S-CKO-03051

(*Continued on next page*)

Continued		
REAGENT or RESOURCE	SOURCE	IDENTIFIER
Oligonucleotides		
Primers for qRT-PCRs, see Table S6	This paper	N/A
Software and algorithms		
Fiji	Image J	http://fiji.sc; RRID: SCR_002285
Prism 9	GraphPad	http://www.graphpad.com; RRID: SCR_002798
ANY-maze	Stoelting Co.	http://www.any-maze.com; RRID: SCR_014289
R software	R	http://www.r-project.org; RRID: SCR_001905
DESeq2	Love et al.[43]	http://bioconductor.org/packages/release/bioc/html/DESeq2.html; RRID: SCR_015687
ClusterProfiler	Yu et al.[44]	http://bioconductor.org/packages/release/bioc/html/clusterProfiler.html; RRID: SCR_016884
Cytobank	Cytobank	http://community.cytobank.org/; RRID: SCR_014043
FlowSOM	Gassen et al.[45]	http://github.com/SofieVG/FlowSOM; RRID: SCR_016899
Rphenograph	Levine et al.[46]	http://github.com/JinmiaoChenLab/Rphenograph; RRID: SCR_022603
FlowJo	TreeStar	http://www.flowjo.com/solutions/flowjo; RRID: SCR_008520
Immunarch	ImmunoMind	https://immunarch.com; RRID:SCR_023089

RESOURCE AVAILABILITY

Lead contact

Further information and requested for resources and reagents should be directed to and will be fulfilled by form lead contact, Kejia Wang (wangkejia@xmu.edu.cn).

Materials availability

Plasmids, cell lines and mice generated in this study should be directed to and will be fulfilled by the lead contact author with a completed Materials Transfer Agreement.

Data and code availability

- All data supporting the finding of this study are available within the paper (and its Supplemental information files). The bulk RNA-seq and IR-seq sequencing raw data have been deposited in the NGDC GSA database: CRA004392, HRA002120. All sequencing data are publicly available as of publication. Accession number is listed in the key resources table.
- This study does not generate any original code.
- Any additional information required to reanalyze the data reported in this work paper is available from the lead contact upon request.

EXPERIMENTAL MODEL AND SUBJECT DETAILS

Subjects

Males constitute a much higher proportion of patients with opioid use disorder in China than females, accounting for 88.3% of the patients.[47] Twenty-one patients with opioid use disorder (18 male and 3 female; mean age = 40.7 ± 9.0 years) were enrolled from the Xi'an Lantian Compulsory Isolated Detoxification Center (Xi'an, China). Diagnoses and clinical interviews were conducted by two senior psychiatrists according to the International Classification of Diseases10th Edition (ICD-10) criteria for opioid dependence.

Participants were included if they (i) were daily or nearly daily users of opioids for a minimum of one year prior to assessment, (ii) were 2-3 days after withdrawal, (iii) never received any antidepressant, antipsychotic drug or mood stabilizer for at least two weeks prior to the study, and (iv) never received methadone maintenance treatment. The Observation Withdrawal Syndrome Scale (Table S5) used in the present study was provided by Xi'an Mental Health Center (Xi'an, China). The overall score including 4 grades are 52. The Withdrawal Symptoms Scale was performed by an experienced psychiatrist. The opioid addiction phenotypes were obtained according to the patient's self-report including education level, marital status, occupation status, average income, family relationship, cumulative duration, age of onset, duration from first drug use to addiction (DFDUA), average dose, route of drug use, body weight, appetite, memory, libido, withdrawal score and the number of withdrawal times.

Participants were excluded if they had a history of amphetamine, ketamine, barbiturate, benzodiazepine, marijuana, or other drug addiction (nicotine and alcohol) according to ICD-10, bipolar disorder, schizophrenia, or were taking other prescribed medications that could affect the CNS.

Twenty healthy controls (17 male and 3 female; mean age = 35.8 ± 3.6 years) were from the Health Examination Center of the First Affiliated Hospital of Xi'an Jiaotong University. The inclusion criteria for controls were: no drug or alcohol dependence. Subjects with a personal or family history of mental illness, or Axis I disorder diagnosed according to the MINI-International Neuropsychiatric Interview were excluded from the control group.

All participants were also excluded if they: were taking other prescribed medications that could affect the CNS; had a history of seizures, hematological diseases, or severe lung, liver or kidney impairment; chronic infections, malignancies, autoimmune diseases and hyperthyroidism. All participants were asked to provide written informed consent; our study protocol was approved by the Medical Ethics Committees of Xi'an Jiaotong University (NO. 2021–1463).

Animals

Foxp3$^{YFP\text{-}cre}$ mice (The Jackson laboratory) were crossed with *Ifng*^{loxP} (Cyagen) and *Ccr2*^{loxP} (Gempharmatech) mice for generation of *Ifng*^{cKO} and *Ccr2*^{cKO} mice. *Ifng*^{loxP} and *Ccr2*^{loxP} mice were used as control in this study. Male mice (C57BL/6J background) between 6-8 weeks of age were used for animal experiments. All mice were housed in pathogen-free animal rooms under controlled conditions [12-hour light/dark cycle, 50 ± 5% humidity and 22 ± 3°C] with food and water provided *ad libitum* at the Animal Care Centre of Xi'an Jiaotong University/Xiamen University. All animal experiments were approved by the Committee on Animal Care and Use of the above-mentioned university and performed according to the guidelines of national regulations. For *in vivo* blocking of IFN-γ, mice were intraperitoneally injected every third day with 200 μg/dose anti-mouse IFN-γ (clone XMG1.2, Bio X cell).

METHOD DETAILS

Morphine and heroin treatments

HCL-morphine and HCL-heroin (The Third Research Institute of The Ministry of Public Security, Shanghai, China) were prepared in 0.9% sodium chloride. Morphine treatment was performed as previously described.[48] The mice received two daily intraperitoneal injections of saline or escalating doses of morphine from 10 to 50 mg/kg for 7 days or 5 to 10 mg/kg for 28 days or heroin 1 to 2 mg/kg for 28 days. The tissue samples were collected 48 hours after the last morphine/heroin injection.

Mass cytometer (CyTOF) and data analysis

Human PBMCs specimens were separated by Ficoll (Solarbio). All samples were processed as described in our previous study.[49] The isolated PBMCs were stained for viability test with 0.5 μM cisplatin (diluted in prewarmed serum-free medium) and then fixed with 1.6% paraformaldehyde for 10 minutes at room temperature. After washing with PBS (containing 0.5% BSA and 0.02% sodium azide), cells were incubated with Fc Receptor Blocking Solution for 10 minutes at room temperature. Subsequently, the cells were stained with antibody cocktail (Table S6) against surface markers and intracellular markers and performed on a CyTOF2 mass cytometer (Fluidigm, Helios). All CyTOF data were normalized by EQ-bead and then uploaded to Cytobank (https://community.cytobank.org/) for data cleaning. The fcs files were used as inputs of the function 'cytof_exprs' with 'cytofAsinh' as the transformation method. FlowSOM (R package, v.1.18.0) was used to cluster the single alive cells with a deep-learning-based clustering. Then, we performed Phenograph (R package, v0.99.1) to cluster the groups' results from FlowSOM, followed by manually annotated these clusters to known immune cell types. Cell type percentage was measured by the number of a certain cell type over total cells from each sample. Foxp3^{high} cells were defined as cells with expression values higher than the mean of total cells, while others were Foxp3^{low} cells. Detailed information is provided in Table S1.

Enzyme-linked immunosorbent assay (ELISA)

ELISA detection was used for IFN-γ, TGF-β, IL-6, IL-10, TNF-α, Ccl2, Ccl19, Ccl21 and IL-17 determination in mice after treatment. All the procedures were performed according to the manufacturer's instructions. All reagents mentioned come from the ELISA kits (Sinobestbio). Samples (including standards of known target protein concentrations and unknowns) were pipetted into these wells. During the first incubation (37°C for 1 hour), the target protein antigen and HRP-labeled detection antibody specific for target protein were simultaneously incubated. After incubation, a substrate solution (TMB) was added to induce a colored reaction product (37°C

for 15 minutes avoiding light). The optical density (O.D.) at 450 nm was measured using a microtiter plate reader within 15 minutes. The intensity of this colored product was directly proportional to the concentration of target protein present in the samples.

Tissue dissociation and flow cytometry

For T cell detection, tissue was gently triturated through a 75-μm gauge stainless steel mesh using a sterile 20 ml syringe plunger in RPMI medium with 10% foetal bovine serum (FBS). The NAc region was dissociated into single cells as previously described.[50] Briefly, the mice were anesthetized with isoflurane, and their brains were rapidly extracted. The NAc was microdissected at its dorsolateral borders and pooled for digestion (three mice per replicate). Pooled tissue samples were dissociated using the papain dissociation system (Worthington) following the manufacturer's instructions, and the dissociation was stopped by dilution with EBSS #2 containing ovomucoid protease inhibitor. Subsequently, the resulting cell suspension was filtered through a 20-μm filter and washed with cold HBSS solution (Solarbio).

The isolated cells were incubated with fluorescently conjugated antibodies directed against human PerCP-CD3 (clone: HIT3a), PE-CD8a (clone: HIT8a), PE-Foxp3 (clone: 150D), FITC-CD4 (clone: A161A1), FITC-CD19 (clone: HIB19), PE-HLA-DR (clone: LN3), FITC-CD56 (clone: HCD56), PE-CD7 (clone: 4H9/CD7), FITC-CD44 (clone: IM7), PE-CD11a (clone: HI111), APC-IFN-γ (clone: 4S.B3); mouse PE-Foxp3 (clone: 150D), APC-IFN-γ (clone: XMG1.2), APC-IFN-γR (clone: MOB-47), APC-T-bet (clone: 4B10), PE-CD8a (clone: 53-6.7) and FITC-CD4 (clone: GK1.5) from BioLegend for 20 minutes at 4°C in the dark. For cytokine detection, the gated cells were sorted and stained with cytokine antibodies after incubation with permeabilization buffer. The stained cells were examined using a BD Aria III machine and analyzed with FlowJo software (TreeStar).

In vitro assays

Splenic Tregs ($CD4^+YFP^+$) from *Foxp3*$^{YFP\text{-}cre}$ mice were sorted and cultured in RPMI supplemented with 10% FBS. The isolated cells were then cultured with 1000 IU IL-2 (novoprotein) and indicated concentration of morphine or heroin for 72 hours. For co-culture assays, the sorted Treg population was seeded into the upper or lower chambers in a 24 well transwell plate (Millipore) with 100 ng/ml of PMA (Sigma), 500 ng/ml of Ionomycin (Sigma), and IL-2 together for 72 hours.

Noninvasive arterial oxygen saturation (SaO_2) measurement

Thirty minutes after morphine injection, continuous SaO_2 data were monitored by using the OXY200 modules of BioPAC MP-160 system and AcqKnowledge software (BIOPAC). The detecting head of the arterial oxygen saturation sensor was glued to mouse paw center with medical tape. The pulse oximeter data were recorded when the tracing showed a steady pulse rate signal and Module Status up to 14.99.

TCR IR sequencing and analysis

Total RNA from NAc tissue was extracted using the RNeasy Mini Kit (Qiagen) according to the manufacturer's specifications. Then, 1 μg of total RNA was reverse-transcribed into cDNA using a Transcriptor First-Strand cDNA Synthesis Kit (Roche Applied Science) with a C1000 Touch™ Thermal Cycler (Bio-Rad). For the construction of the library of the TCR IR, two-round nested amplicon arm-PCR with specific primers was performed as previously described.[51] The first round of PCR was performed with the following program: one cycle of 94°C for 60 sec, 30 cycles of denaturation at 94°C for 30 sec and annealing at 60°C for 60 sec, and the final extension for 10 min at 72°C. For the second round of PCR amplification, a 5 μl template of the first round PCR product was used, and the same PCR protocol was followed in a 50 μl reaction. The amplicons were purified using the AxyPrep DNA Gel Extraction Kit (Axygen Biosciences) and paired-end sequenced (2 × 150 bp) on an Illumina platform according to standard protocols. The sequencing data were harvested by filtering the low-quality sequences and processed using a standard procedure. The V, D, J and CDR3 distribution and diversity algorithms were identified by R package Immunarch.[49,52] Detailed information is provided in Table S3.

Bulk RNA sequencing and gene expression analysis

Total RNA from PBMCs or NAc was extracted using RNeasy Mini Kit (Qiagen). Quantification of RNA concentration was performed by Quantus fluorometer and Quantus RNA HS Assay Kit (Promega). Then, RNA was fragmented at 95°C for 0-15 minutes according to the DV200 value estimated by Agilent 2100 Bioanalyzer System. NEBNext® Ultra™ II Directional RNA Library Prep Kit (NEB) was used for cDNA synthesis and strand-specific library preparation. The libraries were prepared and quantified by a Quantus fluorometer. After pooling, libraries were then sequenced on Illumina NovaSeq 6000 instrument (Illumina) with PE150 strategy. The gene expression estimates were reported as fragments per kilobase of transcript per million mapped reads (FPKM). The DEGs were obtained using the R package DESeq2.[43] The *p* values were adjusted using Benjamini and Hochberg's approach for controlling the false discovery rate (FDR, *q*-value). Genes with a q-value < 0.05 and $\log_2|\text{Fold Change}| > 1$ were deemed to be differentially expressed. A GSEA of Kyoto Encyclopedia of Genes and Genomes (KEGG) pathways and Gene Ontology (GO) terms were performed using the R package ClusterProfiler.[44] Detailed information is provided in Tables S2 and S4.

Spine morphology analysis

Golgi-Cox staining was performed to analyze the possible changes in the morphology of dendritic spines within NAc. The brains were first stored in the dark for 28 days in Golgi-Cox solution and then for 5 days in 30% (wt/vol) sucrose solution. Coronal sections

(200-μm thick) with the NAc were collected using a vibratome. The sections were stained with ammonium hydroxide for 30 minutes, incubated in 20% ammonium hydroxide for 30 minutes and fixed in Kodak Film Fixer for another 30 minutes. The sections were then dehydrated in ethanol, cleared in xylene solution. To improve the accuracy and quality of spine morphology analysis, Z-stacks of Golgi-stained images were captured using a Leica MZFLIII microscope with a 100 × oil immersion objective, then were flattened into a single layer using ImageJ software (Fiji version, https://imagej.net/software/fiji/) as shown in Figure S4I.[53–55]

The MSNs in NAc were identifiable based on their characteristic morphology (~20-μm-diameter soma, dendrites that taper and become heavily laden with spines).[56] The spine analysis was performed using secondary dendrites with a length greater than 20 mm. The dendritic spines were classified into four different types: mushroom-like spines (the diameter of the heads was markedly greater than that of the necks), thin-like spines (the length of the spines was greater than the diameter of the necks with no apparent heads), stubby-like spines (the diameter of the necks was similar to the total length of the spines without detectable heads) and branched-like spines (the spines had two or more heads).[14] In addition, approximately 10% of the spines could not be classified into any of these categories. The density of dendritic spines (10 μm), the distribution of different spine types, and the ratio of each type of dendritic spine were analyzed. For each mouse, more than 10 random dendritic branches from different neurons were chosen. All images were manually coded and randomized for a subsequent blind analysis, which was performed by two researchers independently.

Analysis of the synaptic ultrastructure

Electron microscopic studies were conducted to analyze the possible changes in the synaptic ultrastructure within NAc. The procedure used for TEM was previously described.[57] Following anesthetization with 10% chloral hydrate, the mice were perfused transcardially with saline and then with 0.1 M phosphate buffer (PB; pH 7.4) containing 4% paraformaldehyde and 0.25% glutaraldehyde. Their brains were removed immediately and stored in 0.1 M PB (pH 7.4) with 4% paraformaldehyde and 2.5% glutaraldehyde at 4°C. The NAc was then extracted and dissected into ~1-mm^3 pieces. The samples were fixed in a fresh solution of 1% osmium tetroxide for 90 minutes, dehydrated in ethanol and embedded in Epon-Araldite resin. Ultrathin sections were cut and placed onto grids, stained with 2% aqueous uranyl acetate, counterstained with 0.3% lead citrate, and the electron microscope images (magnification 30,000×) were captured using a Hitachi 7650 electron microscope operated at 80 kV.

Synapses were identified by clear pre- and postsynaptic membranes and the presence of synaptic vesicles in the presynaptic terminal. The number of asymmetrical and symmetrical synapses, the thickness of the postsynaptic density (PSD) at the thickest part in asymmetrical synapses and the length of active zone and the width of the synaptic cleft in asymmetrical and symmetrical synapses were measured. Quantification was achieved using 20 random images per mouse. All electron microscope images were manually coded and randomized for a subsequent blind analysis, which were performed by two researchers independently.

RNA isolation and qPCR

RNA isolation, reverse transcription, and qPCR were performed as described previously.[58] The total RNA of isolated cells or tissue were extracted using sterile steel balls and TRIzol (Invitrogen). The RNA was dissolved in chloroform and precipitated by isopropyl alcohol. First-strand complementary DNA was synthesized using a Transcriptor First Strand cDNA Synthesis Kit (LABLEAD, Beijing, China) according to the manufacturer's recommendations. Subsequently, the quantitative real-time PCR was performed using Hieff® qPCR SYBR Green Master Mix (Yeasen Biotechnology) on CFX96® Real-Time System (Bio-Rad). The relative expression (fold) was calculated using the comparative method $2^{-\Delta\Delta Ct}$ method. The mRNA expression was analyzed based on the fold change relative to GAPDH expression. The relative mRNA level was determined as the experimental level relative to the control level. The primer sequences were designed by AuGCT Biotechnology Corp., Ltd. (Beijing, China), and are shown in Table S6.

Immunoblotting

Protein lysates were prepared in RIPA buffer (Solarbio) containing protease and phosphatase inhibitors (Bimake). The total protein concentrations were determined using a BCA Protein Assay Kit. The proteins were separated by sodium dodecyl sulfate polyacrylamide gel electrophoresis (SDS-PAGE) and transferred to PVDF membranes (Millipore), and the membranes were then incubated with primary antibodies against Hif1α (Solarbio; 1:1000), phospho-Akt (S473, Solarbio; 1:1000), pan-Akt (Solarbio; 1:1000), Foxo3a (Solarbio; 1:1000), Foxo1 (Solarbio; 1:1000), Fabp7 (Abcam; 1:1000), Ifngr1 (Servicebio; 1:1000), Rip3 (Cell Signaling Technology; 1:1000), phospho-Rip3 (Abcam; 1:1000) and Tubulin (Cell Signaling Technology; 1:2000) overnight at 4°C. After incubation with the corresponding secondary antibodies, the protein bands were visualized by the addition of the HRP membrane substrate (Millipore) and then scanned using Bio-Rad ChemiDoc Touch (Bio-Rad).

Immunohistochemistry

The mice were deeply anesthetized with isoflurane and intracardially perfused with 4% paraformaldehyde in 0.1 M PB (pH 7.4). The brains were immediately removed and postfixed in 4% paraformaldehyde, and then were embedded in paraffin as described previously.[20] For immunohistochemical bright field staining, after neutralized endogenous peroxidases, the sections were incubated with primary antibodies at 4°C overnight, then the staining was performed according to the manufacturer's protocol using Enhanced Polymer Detection System (ZSGB-BIO). For immunofluorescence staining, the sections were blocked with normal donkey serum. To obtain the results shown in Figure 6C, the following procedure was repeated for multiple immunostaining: (1) incubation with the

primary antibody (rabbit anti-Fabp7, mouse anti-IBA1 and mouse anti-GFAP in tune) overnight at 4°C; (2) incubation with the HRP-conjugated secondary antibodies (which appropriately respond to the species of the primary antibody) at room temperature for 50 minutes; (3) incubation with fluorescein-conjugated tyramide signal amplification (TSA) (cy3-Tyramide, FITC-Tyramide, or iF647-Tyramide) at room temperature for 10 minutes; and (4) microwave treatment to remove the primary and secondary antibodies combined with tissue. Finally, the sections were incubated with the last primary antibody (mouse anti-NeuN) and appropriate species-specific 594-labeled fluorescence secondary antibody. To obtain the other results, the sections were incubated with primary antibodies at 4°C overnight, and then incubated with secondary antibodies 2 hours at room temperature. Primary antibodies were used as following: rabbit anti-CD4 (Abcam; 1:100), rabbit anti-Foxp3 (Servicebio; 1:100), rabbit anti-CD19 (Servicebio; 1:200), rabbit anti-NK1.1 (Abcam; 1:200), rat anti-Ly6c (Abcam; 1:200), mouse anti-NeuN (Cell Signaling Technology; 1:200), rabbit anti-NeuN (Servicebio; 1:200), rabbit anti-CD31 (Servicebio; 1:200), rabbit anti-Ccl2 (Servicebio; 1:100), mouse anti-Stat1 (Proteintech; 1:200), rabbit anti-Fabp7 (Abcam; 1:200), mouse anti-c-Fos (Abcam; 1:200), mouse anti-GFAP (Servicebio; 1:200) and mouse anti-IBA1 (Servicebio; 1:200). Secondary antibodies used included the following: FITC-Tyramide (Servicebio; 1:500), cy3-Tyramide (Servicebio; 1:500), iF647-Tyramide (Servicebio; 1:500), Alexa488-conjugated donkey anti-mouse IgG (Abcam; 1:500), Alexa594-conjugated donkey anti-rabbit IgG (Abcam; 1:500) and Alexa647-conjugated donkey anti-mouse IgG (Abcam; 1:500). In addition, for the determination of cell apoptosis, the TUNEL Cell Apoptosis Detection Kit (Servicebio) was used according to the manufacturer's instructions. The nuclei were stained with DAPI. The images of the processed sections were scanned using a Panoramic (3DHISTECH) Digital Slide Scanner. All images were manually coded and randomized for a subsequent blind analysis, which was performed by two researchers independently.

Analysis of the permeability of the BBB

The BBB permeability was detected by measuring EB extravasation. Two hours after the EB (Sigma-Aldrich) (2% wt/vol) injection (4 ml/kg, i.p.), the mice were deeply anesthetized and transcardially perfused with saline until colorless perfusate was observed to remove the intravascular EB, and the brains were then immediately removed. For EB fluorescence, the brains were postfixed in 4% paraformaldehyde overnight at 4°C, dehydrated with 30% sucrose (wt/vol), and then frozen in OCT compound. Coronal sections (10-μm thick) were cut on a cryostat. After vascular endothelial cells were marked with anti-CD31 (Servicebio; 1:200), the sections were scanned using a Panoramic (3DHISTECH) Digital Slide Scanner. For EB quantification, the NAc was collected, rapidly weighed, and homogenized in PB (pH 7.4). The supernatant was incubated in an equal volume of trichloroacetic acid overnight at 4°C. After centrifugation, the concentration of EB was determined at 620 nm by spectrophotometric analysis according to a standard curve.

Stereotaxic injections

The mice were anesthetized with isoflurane, fixed in a stereotaxic apparatus, and maintained under anesthesia with around 2.5% isoflurane. Using the bregma as a reference point, the stereotaxic coordinates of NAc (AP -1.4 mm, ML ± 2.0 mm, DV -4.6 mm, 10° angle) and PVT (AP -1.5 mm, ML 0.5 mm, DV -3.2 mm, 10° angle) were used. AAV-TRE-scrambled (OBiO Technology), AAV-TRE-shRNA (Ifngr1) (target sequence: GCCAGAGTTAAAGCTAAGGTT; OBiO Technology), AAV-hSyn-rTTA (OBiO Technology), AAV-TRE-EGFP (Brain VTA Biotechnology), AAV-TRE-Fabp7-EGFP (NM_021272.3; Brain VTA Biotechnology), AAV-GFAP-rTTA (Brain VTA Biotechnology), AAV (Retro)-hSyn-Cre (Brain VTA Biotechnology), AAV-CaMKIIa-DIO-hM4Di-mCherry (Brain VTA Biotechnology), AAV-hSyn-hM4Di-mCherry (Brain VTA Biotechnology) or FG (Fluorochrome) were infused into NAc. A volume of around 200 nl of virus was infused bilaterally into NAc using a calibrated glass microelectrode attached to a 1-μl Hamilton microsyringe at a flow rate of 30 nl/minute. The injector was removed from the brain 10 minutes after the infusion. Fifteen to thirty minutes before behavioral procedure, mice were given 200 nl intracranial injections of either 0.9% isotonic saline or Clozapine N-oxide (300 mM; SIGMA) at a rate of 100 nl/minute. Following surgery, the mice were singly housed for 48 hours and then returned to their home cage. The mice were treated with doxycycline (Dox) (2% in water, MedChemExpress) 4 weeks after viral fusion to trigger transgene expression.

Conditioned place preference (CPP)

A three-stage CPP procedure that contains acquisition, extinction and reinstatement was used in this study. For acquisition, the mice were allowed to move freely between the two compartments for 15 minutes to achieve habituation on day 1. On day 2, the mice were allowed to explore both sides to determine their baseline preference (preconditioning), and the time spent on each side was recorded. During the preconditioning phase, mice that spent more than 600 seconds of the 15-minute period in either chamber or crossed between the chambers fewer than 20 times were excluded from the analysis. On days 3, 5, 7, 9, the mice were injected with morphine (10 mg/kg) or saline (control group) before being confined to compartment A for 45 minutes. On days 4, 6, 8, 10, all the mice (control and morphine groups) were injected with saline and then confined to compartment B for 45 minutes (conditioning). On the test day (day 11), the mice were allowed to freely explore the chambers for 15 minutes without injections. The time spent in each chamber was determined using a video tracking system. During extinction training, all the mice were given saline (i.p., 10 ml/kg) once daily and were immediately confined to the chambers for 30 minutes. After 7 days of extinction training, the place preference was tested by allowing the mice to freely explore the CPP chambers for 15 minutes. Twenty-four hours later, if no CPP effect was detected, the mice were challenged with morphine injection once (i.p., 5 mg/kg) and then subjected to a place preference test (reinstatement test). In each place preference test, the mice were randomly placed on either side of the apparatus.

Spontaneous morphine withdrawal monitoring

Opioid withdrawal in humans often results from cessation or reduction of opioid use, rather than blockade of opioid receptors, and this process can also be modeled in mice. Spontaneous withdrawal syndrome tests were performed as described by previously.[59–61] In the first time, the somatic signs were quantified by direct observation from 12 to 72 hours after the last saline or morphine injection. The somatic signs were recorded 48 hours after morphime withdrawal in subsequent experiments. Mice were individually placed in a transparent plexiglas cylinders (30 cm diameter, 50 heights) for 30 minutes, and withdrawal syndromes were scored by an experimenter who was blinded to the treatment conditions. Jumping and wet dog shake behaviors were recorded as number of events occurring during the total test time; body tremor and diarrhea events were recorded as number of 5 minutes intervals in which they occurred (maximal score = 6). Body weights were measured immediately before and after each 30 minutes test session, and percentage of body weight loss during the test was calculated. For each mouse, a global morphine withdrawal score was also calculated by summating the values obtained for each sign. For this purpose, 1 point was assigned to every 2 wet dog shakes or 2 jumps, absolute value of weight loss was used as a sign to represent body weight change, whereas all other signs were given the absolute values recorded during the test.

QUANTIFICATION AND STATISTICAL ANALYSIS

Statistical analyses were conducted using GraphPad Prism 9.0 (GraphPad Software Inc.) and R 4.1 (https://cran.r-project.org/) software. Parametric tests were applied when normality was satisfied; otherwise, nonparametric tests were used (Mann-Whitney test or Kruskal-Wallis with Dunn's post hoc test). For parametric tests, when homogeneity of variance assumptions was satisfied, unpaired t-test or two-way ANOVA with Bonferroni's post hoc test was used; otherwise, Welch's t-test or Brown-Forsythe and Welch ANOVA with Dunnett T3 post hoc test was used. For two-way ANOVA, the drug treatment, transgene, and gene regulation were considered independent effects and were analyzed accordingly. The repeat measures two-way ANOVA with Bonferroni's post hoc test was used to assess the time series data (Figures S2L, S5J and S5K). The χ^2 test was used for the distribution of different spine types. In addition, the bivariate correlation (Spearman: Figures 1N, S1I and S1J; Pearson: Figures 1P, 6B and S7M) and the partial correlation (Spearman: Figure 1O) analyses were performed to determine the possible correlation. The type I error rate was set to $\alpha = 0.05$ (two-tailed) in all comparisons. The investigators were blinded to the allocation of the groups and the outcome assessments in all experiments. p values less than 0.05 were considered statistically significant. Detailed statistics are provided in Table S7.

Supplemental figures

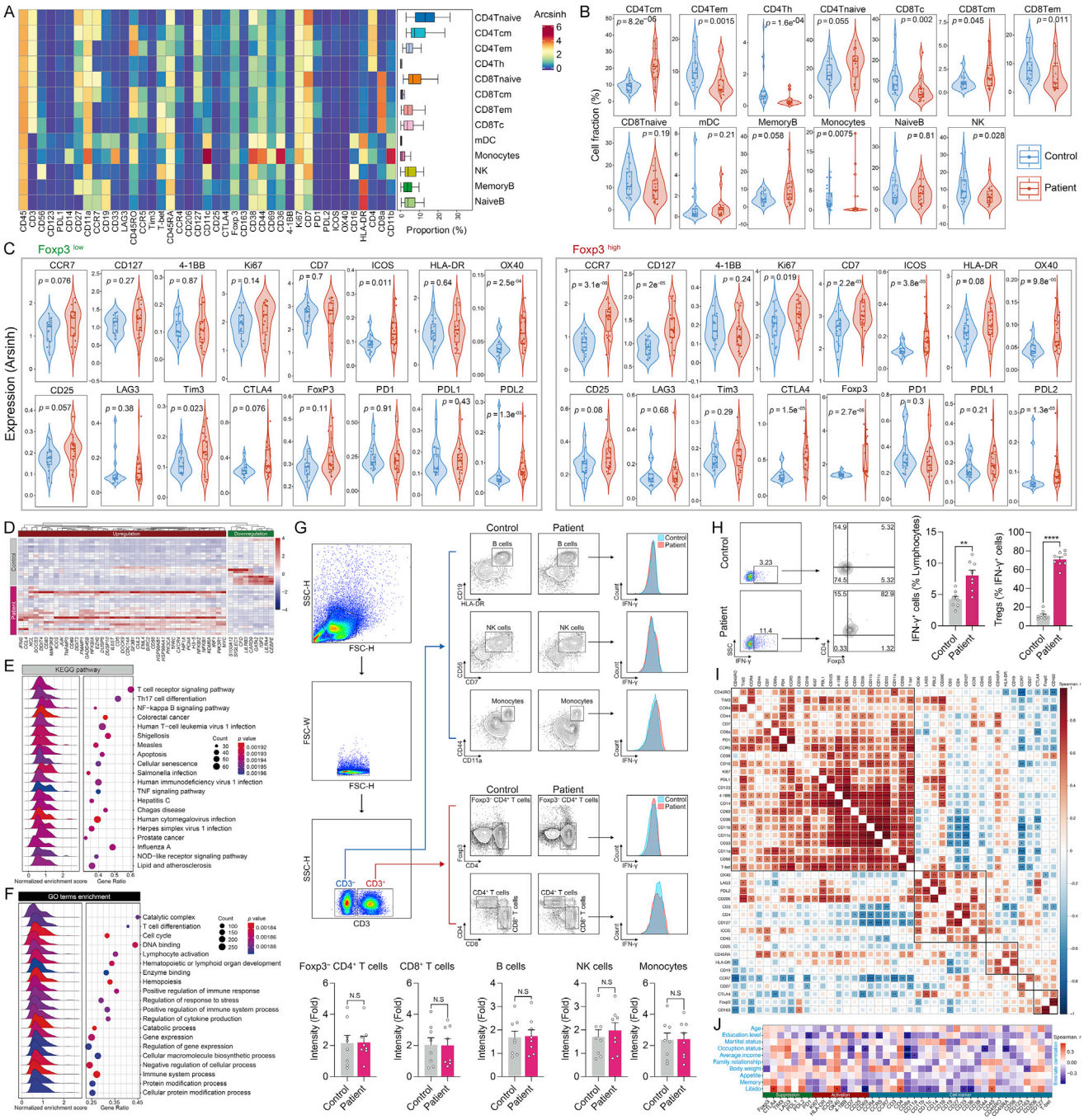


Figure S1. CyTOF and RNA-seq reveal abnormal immune changes in patients with opioid use disorder

(A) Heatmap showing the expression of markers for 13 cell clusters. The proportions are displayed to the right (n = 41).

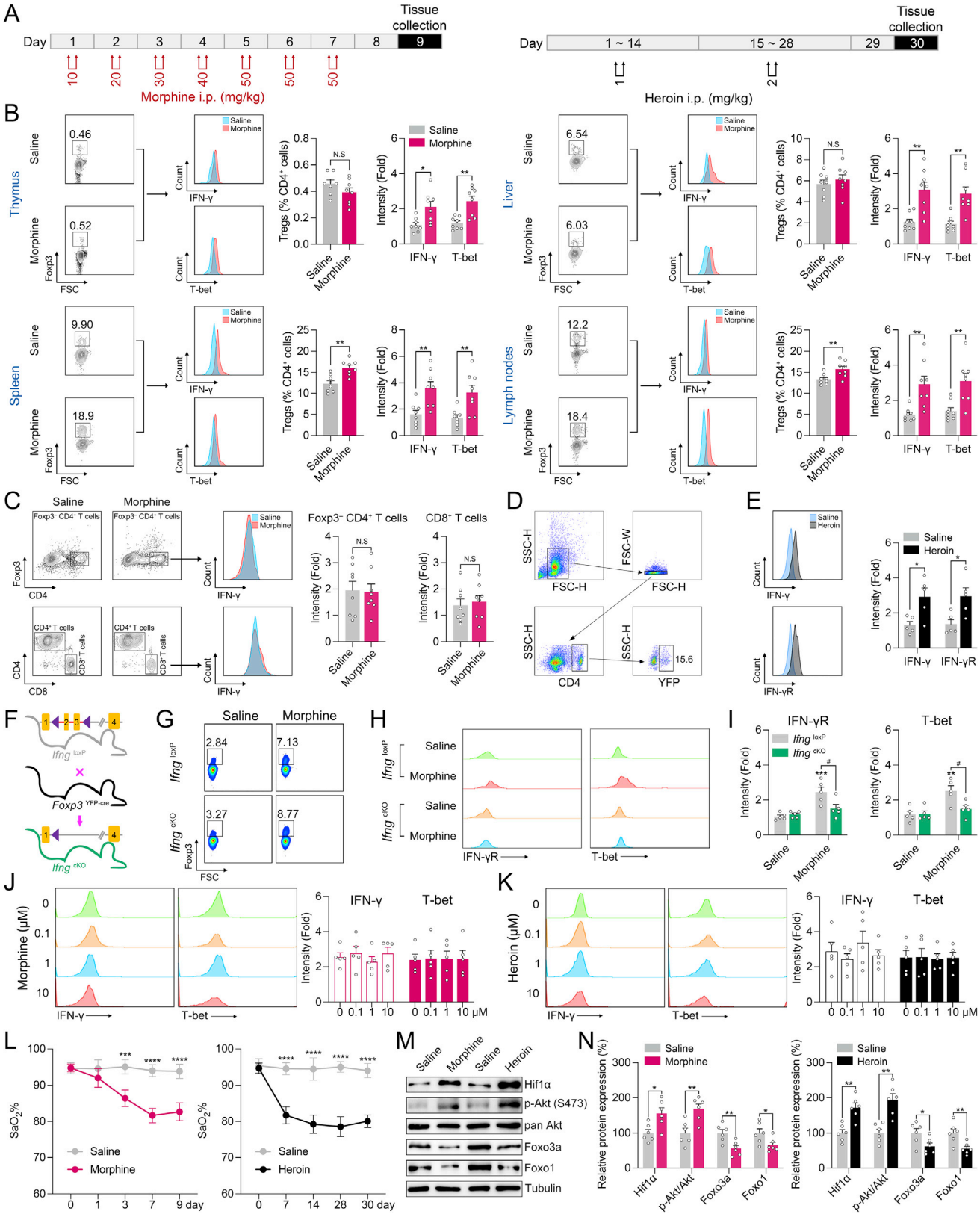
(B) Comparison of the fraction of immune cell subsets (n = 20, 21).

(C) Comparison of the expression of indicated markers in the Foxp3^{low} or Foxp3^{high} population (n = 20, 21).

(D) Heatmap of differentially expressed genes (DEGs) (top 50) in PBMCs by bulk RNA-seq (n = 20, 21).

(legend on next page)

(E and F) Ridge and dot plots of 20 most significant enrichment pathways from (E) GSEA-KEGG pathways and (F) GSEA-GO terms. The colored intensity of peaks and dots indicating enrichment significance. The size representing the number counts in a certain pathway. Normalized enrichment score indicating the analysis results across gene sets (n = 20, 21).
(G) Gating strategy defining Foxp3$^-$ CD4$^+$ T cells, CD8$^+$ T cells, B cells, NK cells, and monocytes from PBMCs (upper). The fluorescence intensity of IFN-γ in indicated cell subsets (lower) (n = 8).
(H) PBMCs samples were isolated from peripheral blood and stained for IFN-γ, CD4, and Foxp3. Representative flow plots (left) and quantification (right) of percent of IFN-γ$^+$ cells in lymphocytes and Tregs in IFN-γ$^+$ cells (n = 8).
(I) Spearman's correlation matrices for CyTOF markers expression (n = 21).
(J) Spearman's correlation between CyTOF markers expression and other traits in patients with opioid use disorder (n = 21).
(B and C) Violin plots showing the distribution of arcsinh-transformed marker expression values, boxplots inside violin plots are shown as the median ± 25%–75% quantiles, and whiskers denote 1.5× interquartile range (IQR); (G and H) Data are shown as the mean ± SEM. Data represent four to five independent experiments. $^{**}p < 0.01$, $^{****}p < 0.0001$.
See also Figure 1.



(legend on next page)

Figure S2. Opioid-mediated global hypoxia results in fragile-like Treg transformation

(A) Flow chart of morphine or heroin administration.

(B) The mice were treated with morphine as described in Figure S2A. $CD4^+$ $Foxp3^+$ Tregs isolated from the thymus, liver, spleen, and abdominal lymph nodes fragility was detected by flow cytometry, respectively. Representative flow plots (left), histogram plots (middle), and quantification (right) of percent of Tregs, the intensity of IFN-γ, and T-bet (n = 8).

(C) Representative plots of $Foxp3^-$ $CD4^+$ T cells and $CD8^+$ T cells in PBMCs by flow cytometry (left). The fluorescence intensity of gated IFN-γ (right) (n = 8).

(D) Gating strategy of splenic Tregs ($CD4^+$ YFP^+) cells from *Foxp3*$^{YFP\text{-}cre}$ mice.

(E) The mice were treated with heroin as described in Figure S2A. Splenic Tregs were isolated, stimulated with PMA, ionomycin, and IL-2, co-cultured for 72 h (see Figure 2B). Representative histogram plots (left) and quantification (right) of the intensity of IFN-γ and IFN-γR (n = 5).

(F) Schematic of generation of *Ifng*^{cKO} mice.

(G–I) The *Ifng*^{loxP} and *Ifng*^{cKO} mice were treated with morphine as described in Figure S2A. $CD4^+$ $Foxp3^+$ Tregs isolated from PBMCs were measured by flow cytometry. Representative (G) flow plots, (H) ridge plots, and (I) quantification of the intensity of IFN-γR and T-bet (n = 5).

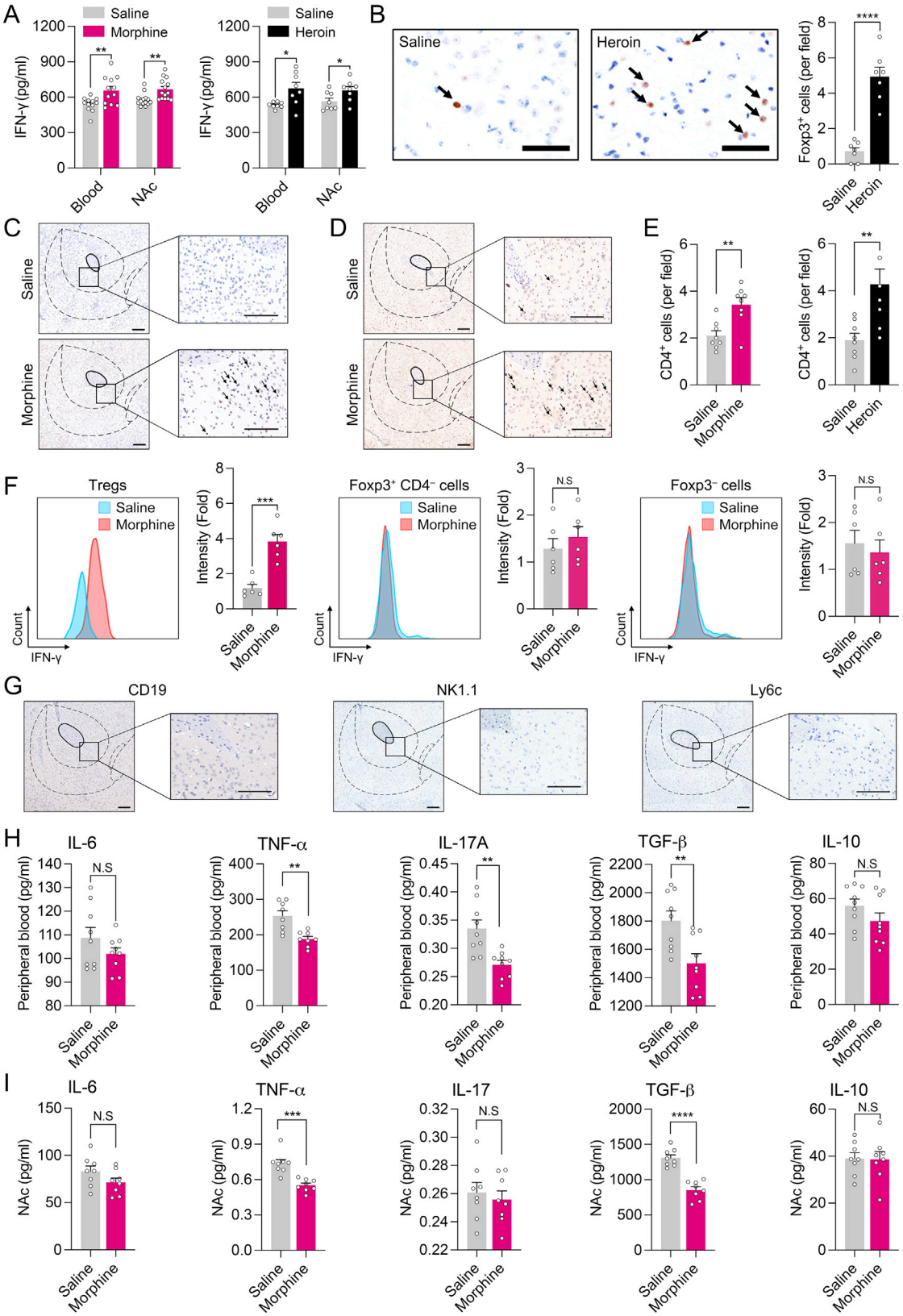
(J and K) Splenic Tregs ($CD4^+$ YFP^+) were isolated from *Foxp3*$^{YFP\text{-}cre}$ mice, treated with IL-2 and different concentrations of (J) morphine or (K) heroin, co-cultured for 72 h. Representative ridge plots (left) and quantification (right) of the intensity of IFN-γ and T-bet (n = 5).

(L) The mice were treated with opioids as described in Figure S2A. The curve plot showing the SaO_2% of mice on the day indicated after morphine (left) or heroin (right) treatment (n = 6).

(M and N) The immunoblots of Hif1α, p-Akt (S473), pan-Akt, Foxo3a, Foxo1, and Tubulin in splenic Tregs from mice noted. (M) Representative immunoblots. (N) The relative expression of the indicated proteins (n = 6).

Data are shown as the mean ± SEM. Data represent three to five independent experiments. $^*p < 0.05$, $^{**}p < 0.01$, $^{***}p < 0.001$, $^{****}p < 0.0001$ compared with saline group (B, E, and N), saline × *Ifng*^{loxP} group (I) or saline group at the same time point (L); $^{\#}p < 0.05$.

See also Figure 2.



(legend on next page)

Figure S3. Opioid exposure triggers fragile-like Treg infiltration

(A) ELISA analysis of IFN-γ in blood or in NAc after morphine (left) (n = 12, 14) or heroin (right) (n = 8) administration.

(B) Representative images (left) and quantification (right) of Foxp3 immunoreactivity in NAc (n = 7); scale bars, 50 μm.

(C and D) Representative images of (C) Foxp3 and (D) CD4 immunoreactivity in NAc; scale bars, 250 μm (low magnification) and 100 μm (high magnification).

(E) Quantification of $CD4^+$ cells per high-power field in NAc after morphine (left) (n = 8) and heroin (right) (n = 6, 8) treatment.

(F) The fluorescence intensity of IFN-γ in $CD4^+$ $Foxp3^+$ Tregs, $Foxp3^+$ $CD4^-$ cells, and $Foxp3^-$ cells as shown in Figure 2D (n = 6).

(G) Representative images of CD19 (left), NK1.1 (middle), and Ly6c (right) immunoreactivity in NAc after morphine treatment. Scale bars, 250 μm (low magnification) and 100 μm (high magnification).

(H and I) The levels of IL-6, TNF-α, IL-17, TGF-β, and IL-10 in (G) blood and in (H) NAc measured by ELISA (n = 8, 9).

Data are shown as the mean ± SEM. Data represent three independent experiments. *$p < 0.05$, **$p < 0.01$, ***$p < 0.001$, ****$p < 0.0001$.

See also Figure 2.

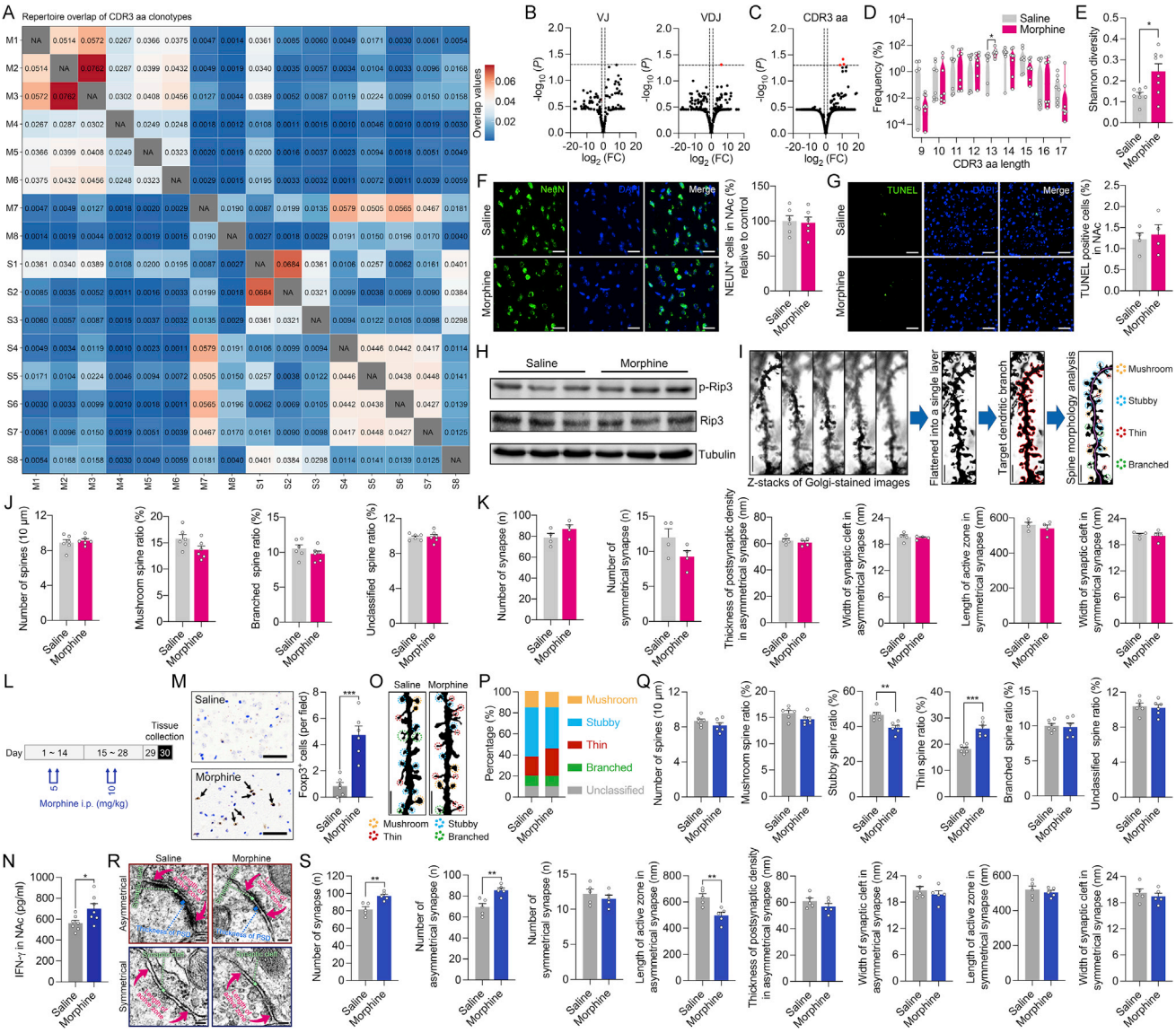


Figure S4. Morphine enhances TCR diversity and reshapes synaptic structure in NAc

(A–E) The profile of TCR β immune repertoire in NAc.

(A) Percentage of overlap of the CDR3 aa clonotypes between each sample (n = 8).

(B) Volcano plots representing the difference in the frequency of VJ (left) and VDJ (right) segments (n = 8).

(C) Volcano plots representing the difference in the frequency of CDR3 aa clonotypes (n = 8).

(D) Violin plots showing the frequency of different CDR3 aa length (n = 8).

(E) Comparison of the Shannon diversity of CDR3 aa (n = 8).

(F) Representative images (left) and quantification (right) of NeuN immunoreactivity in NAc. The values were normalized to those of control mice (n = 6); scale bars, 25 μm.

(G) Representative images (left) and quantification (right) of TUNEL assay results obtained from NAc (n = 4); scale bars, 50 μm.

(H) Western blotting showing the expressions of p-Rip3, Rip3, and tubulin in NAc (n = 3).

(I) Golgi-stained Z stacks images before and after image processing used for spine morphology analysis. A representative Z stacks images summed from different focal fields of all spines on the same dendritic branch (left); processed image clearly shows improved visibility of dendritic spine morphology (right); scale bars, 5 μm.

(J) The density of total spines and the proportions of mushroom- and branched-like and unclassified spines in NAc (n = 6).

(K) The numbers of total and symmetrical synapses, the thickness of the PSD at the thickest part in asymmetrical synapses, the lengths of active zones in symmetrical synapses, the width of the synaptic cleft in asymmetrical, and symmetrical synapses in NAc (n = 4).

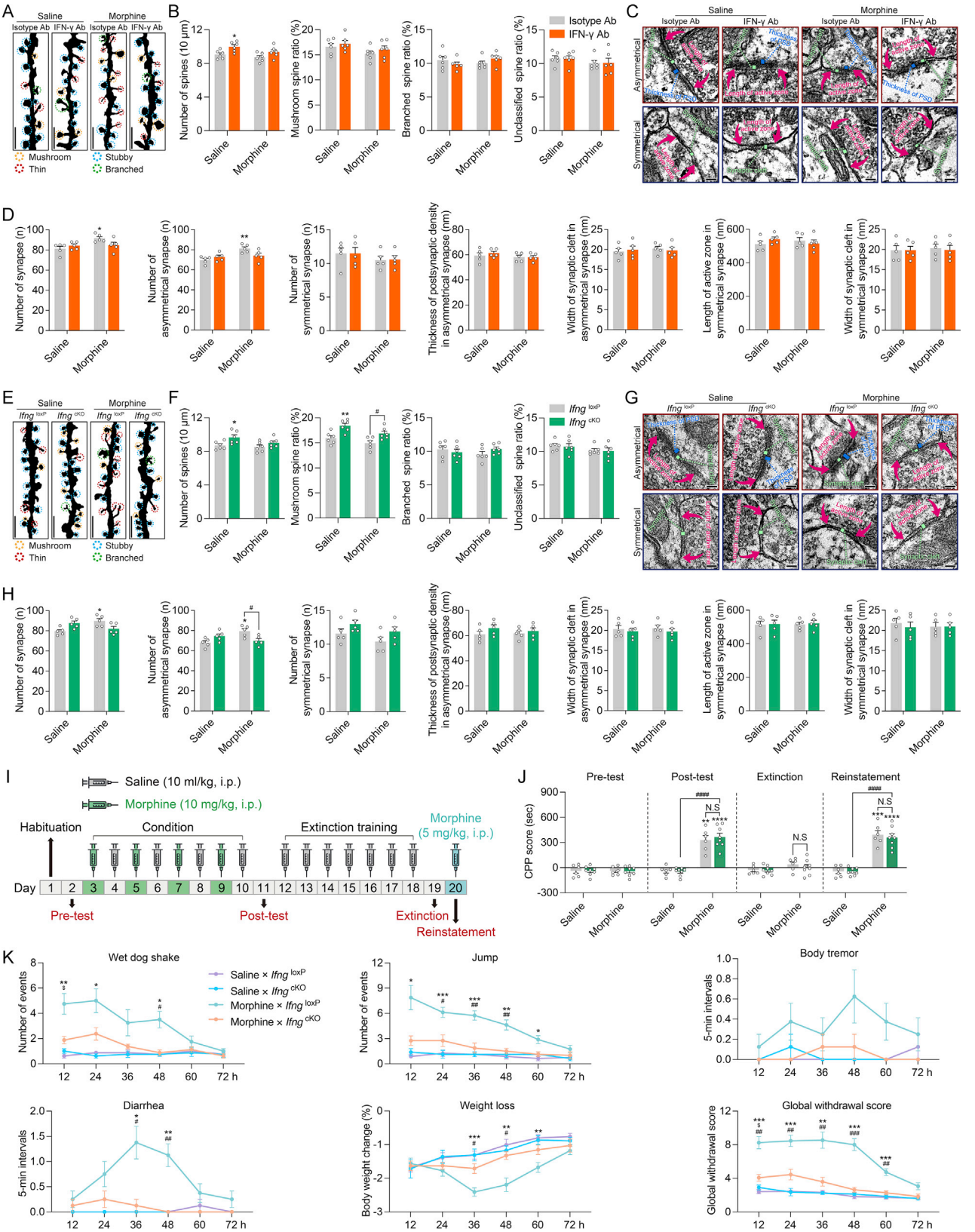
(L) Flow chart of long-term morphine administration.

(M) Representative images (left) and quantification (right) of Foxp3 immunoreactivity in NAc (n = 6); scale bars, 50 μm.

(N) ELISA analysis of IFN-γ in NAc (n = 7).

(legend continued on next page)

(O–S) The effects of long-term morphine treatment on synaptic morphology of NAc by Golgi-Cox staining and TEM.
(O) Representative images of dendritic spines on secondary dendrites of MSNs in NAc; scale bars, 5 μm.
(P) Histograms showing the distribution of different spine types.
(Q) The density of total spines and the proportions of mushroom-like, stubby-like, thin-like, branched-like, and unclassified spines (n = 6).
(R) Representative TEM images; scale bars, 100 nm.
(S) The number of synapses, the number of asymmetrical synapses, the number of symmetrical synapses, the thickness of the PSD at the thickest part in asymmetrical synapses, the lengths of active zones in asymmetrical and symmetrical synapses, and the width of the synaptic cleft in asymmetrical and symmetrical synapses (n = 5).
Data are shown as the mean ± SEM. Data represent three independent experiments. *$p < 0.05$, **$p < 0.01$, ***$p < 0.001$.
See also Figure 2.



(legend on next page)

Figure S5. The effect of IFN-γ deficiency on synaptic structure, related to Figure 3

(A–D) The effects of anti-IFN-γ on morphine-mediated synaptic structure of NAc.

(A) Representative Golgi-Cox staining images; scale bars, 5 μm.

(B) The number of spines, the proportions of mushroom-like, branched-like and unclassified spines (n = 6).

(C) Representative TEM images; scale bars, 100 nm.

(D) The number of synapses, the number of asymmetrical synapses, the number of symmetrical synapses, the thickness of the PSD at the thickest part in asymmetrical synapses, the lengths of active zones in symmetrical synapses, and the width of the synaptic cleft in asymmetrical and symmetrical synapses (n = 5).

(E–H) The effects of *Ifng*^{cKO} on morphine-mediated synaptic structure in NAc by Golgi-Cox staining and TEM.

(E) Representative Golgi-Cox staining images; scale bars, 5 μm.

(F) The density of spines and the proportions of mushroom-like, branched-like, and unclassified spines (n = 6).

(G) Representative TEM images; scale bars, 100 nm.

(H) The number of synapses, the number of asymmetrical synapses, the number of symmetrical synapses, the thickness of the PSD at the thickest part in asymmetrical synapses, the lengths of active zones in symmetrical synapses, and the width of the synaptic cleft in asymmetrical and symmetrical synapses (n = 5).

(I) Flow chart of CPP procedure.

(J) Morphine CPP score in different stages (n = 6, 8).

(K) The withdrawal score for withdrawal symptoms including wet dog shake, jump, body tremor, diarrhea, weight lost, and global withdrawal score (n = 8).

Data are shown as the mean ± SEM. Data represent three to five independent experiments. (B–J) $^{*}p < 0.05$, $^{**}p < 0.01$, $^{***}p < 0.001$, $^{****}p < 0.0001$ compared with saline × isotype Ab group (B and D), saline × *Ifng*^{loxP} group (F and H) or saline × *Ifng*^{loxP} group at the same time point (J); $^{\#}p < 0.05$, $^{\#\#\#\#}p < 0.0001$. (K) $^{*}p < 0.05$, $^{**}p < 0.01$, $^{***}p < 0.001$, morphine × *Ifng*^{loxP} compared with saline × *Ifng*^{loxP} group at the same time point; $^{\$}p < 0.05$, morphine × *Ifng*^{cKO} compared with saline × *Ifng*^{loxP} group at the same time point; $^{\#}p < 0.05$, $^{\#\#}p < 0.01$, $^{\#\#\#}p < 0.001$, morphine × *Ifng*^{loxP} compared with morphine × *Ifng*^{cKO} group at the same time point.

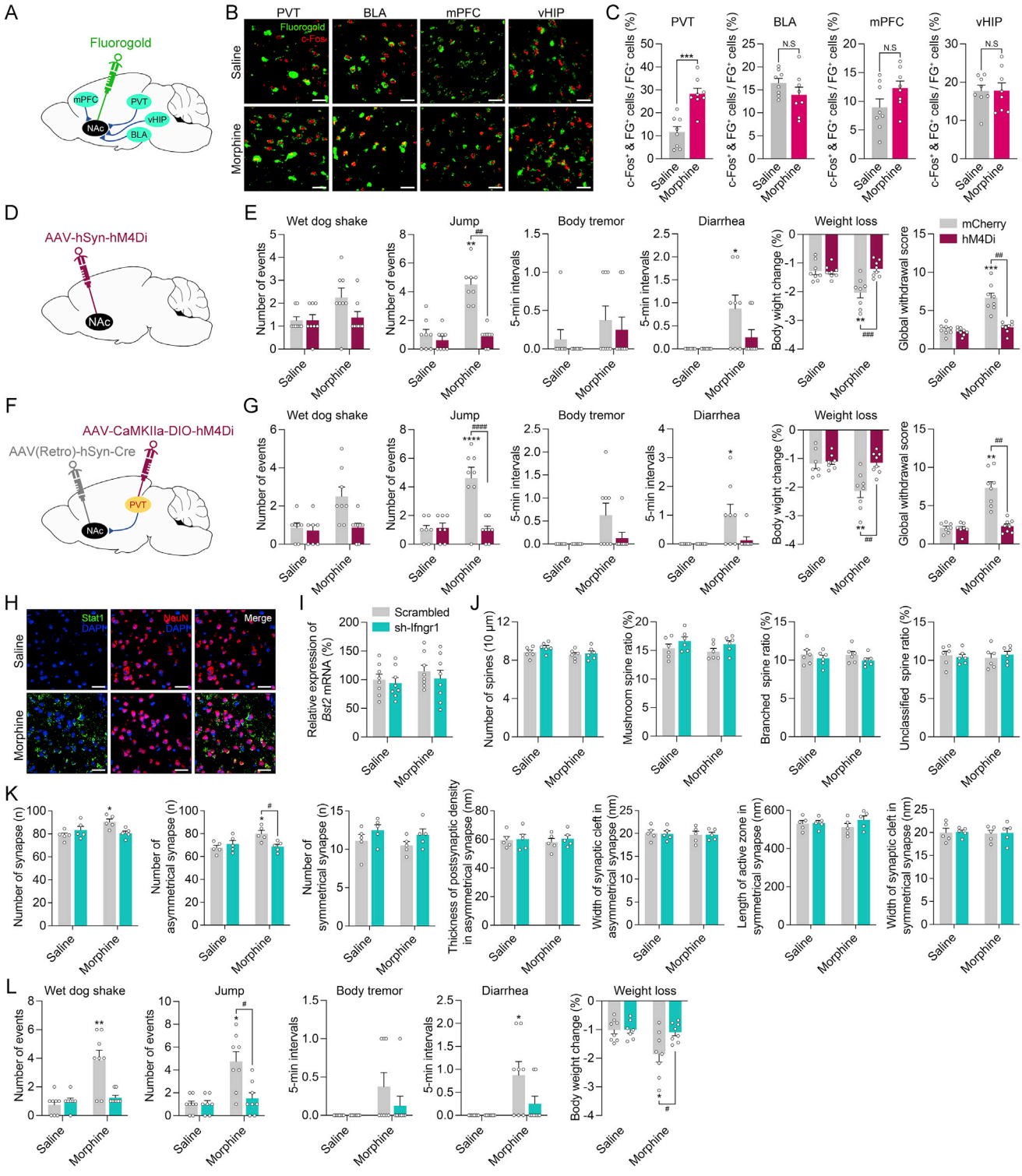


Figure S6. Knockdown of Ifngr1 prevents morphine-induced synaptic damage

(A–C) The afferents to NAc activating test.

(A) The schematic of afferents to NAc.

(B) The co-immunostaining of c-Fos and FG in PVT, BLA, mPFC, and vHIP; scale bar, 25 μm.

(C) Quantification of active c-Fos cells (c-Fos + FG/FG cells) per mm^2 (n = 8).

(D and E) Inhibition of NAc neurons via a chemogenetic approach.

(legend continued on next page)

(D) The schematic of virus injection.
(E) The effect of inhibition of NAc on withdrawal symptoms including wet dog shake, jump, body tremor, diarrhea, weight loss, and global withdrawal score 48 h after the last morphine treatment (n = 8).
(F and G) Inhibition of PVT→NAc projection via a chemogenetic approach.
(F) The schematic of virus injection.
(G) The effect of inhibition of PVT→NAc on withdrawal symptoms including wet dog shake, jump, body tremor, diarrhea, weight loss, and global withdrawal score 48 h after the last morphine treatment (n = 7, 8).
(H) Representative co-immunostaining images for Stat1, NeuN, and DAPI in NAc; scale bars, 25 μm.
(I) The relative expression level of *Bst2* mRNA (n = 8).
(J) The number of spines, the proportions of mushroom-like, branched-like, and unclassified spines (n = 6).
(K) The number of synapses, the number of asymmetrical synapses, the number of symmetrical synapses, the thickness of the PSD at the thickest part in asymmetrical synapses, the lengths of active zones in symmetrical synapses, and the width of the synaptic cleft in asymmetrical and symmetrical synapses (n = 5).
(L) The counts of scores for withdrawal symptoms 48 h after the last morphine treatment (n = 7, 8).
Data are shown as the mean ± SEM. Data represent two to five independent experiments. $^{*}p < 0.05$, $^{**}p < 0.01$, $^{***}p < 0.001$, $^{****}p < 0.0001$ compared with saline group (C), saline × mCherry group (E and G) or saline × scrambled group (I, J, K, and L); $^{\#}p < 0.05$, $^{\#\#}p < 0.01$, $^{\#\#\#\#}p < 0.0001$.
See also Figures 3 and 4.

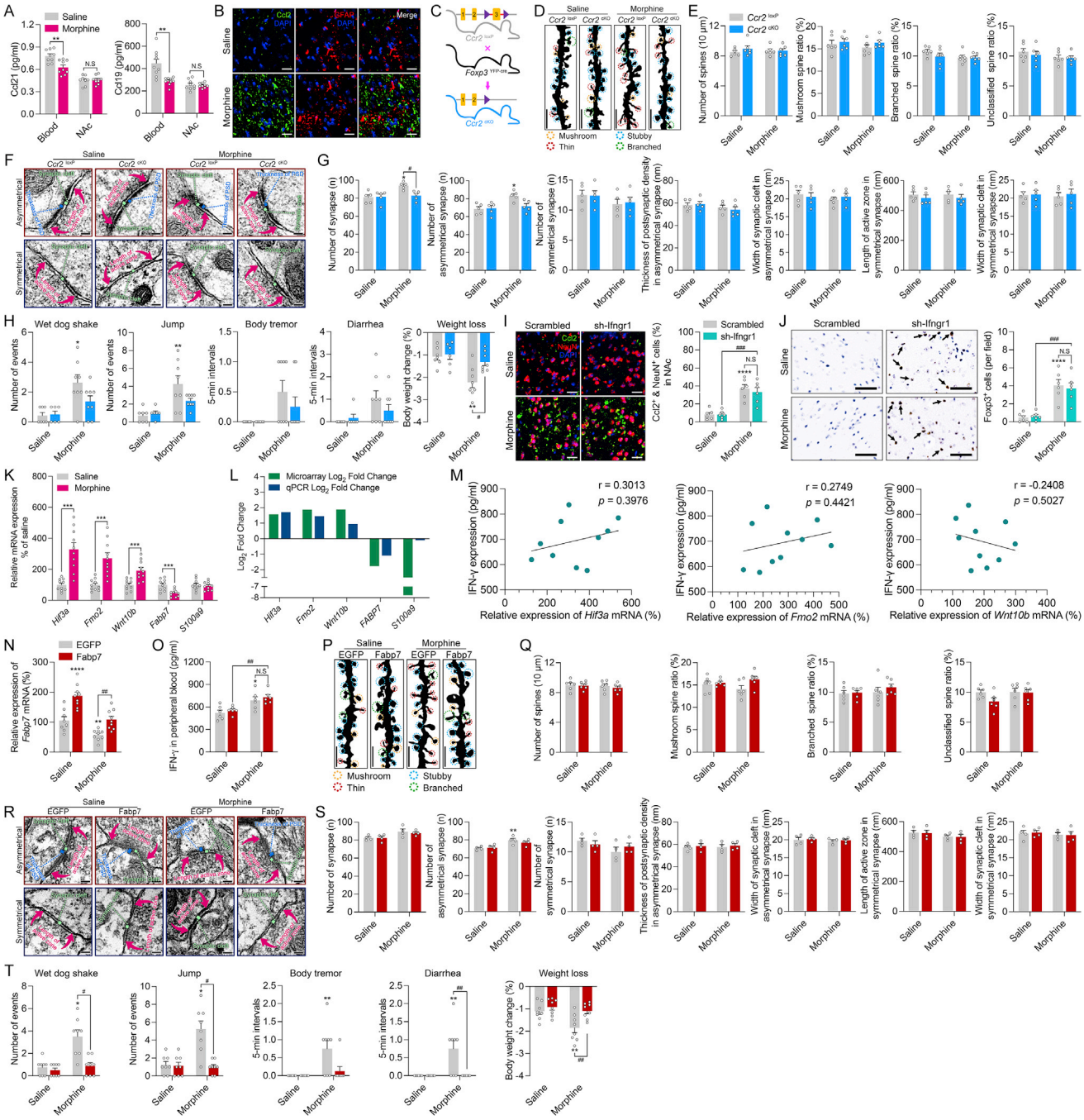


Figure S7. The potential mechanism of morphine-mediated Treg infiltration into NAc

(A) The levels of CCL21 (left) (n = 8, 9) and CCL19 (right) (n = 9) in peripheral blood and NAc determined by ELISA.

(B) Representative co-immunostaining images for Ccl2, GFAP, and DAPI in Nac; scale bars, 25 μm.

(C) The schematic of generation of Foxp3^{+} cell-specific Ccr2 knockout (*Ccr2*^{cKO}) mice.

(D–G) The effects of *Ccr2*^{cKO} on morphine-mediated synaptic structure in NAc by Golgi-Cox staining and TEM.

(D) Representative Golgi-Cox staining images; scale bars, 5 μm.

(E) The density of spines and the proportions of mushroom-like, branched-like, and unclassified spines (n = 6).

(F) Representative TEM images; scale bars, 100 nm.

(G) The number of synapses, the number of symmetrical synapses, the number of asymmetrical synapses, the thickness of the PSD at the thickest part in asymmetrical synapses, the lengths of active zones in symmetrical synapses, and the width of the synaptic cleft in asymmetrical and symmetrical synapses (n = 5).

(H) The counts of scores for withdrawal symptoms 48 h after the last morphine treatment (n = 6, 7, 8).

(legend continued on next page)

(I and J) The mice were treated with morphine as described in Figure 4A.
(I) Representative co-immunostaining images for Ccl2, NeuN, and DAPI in Nac; scale bars, 25 μm (left). The percentage of Ccl2 + NeuN double-labeled cells (right) (n = 6).
(J) Representative images (left) and quantification (right) of Foxp3 immunoreactivity in Nac; scale bars, 50 μm (n = 6).
(K) The relative expressions of the 5 DEGs of interest by qPCR (n = 10).
(L) Comparison of the levels of 5 DEGs of interest between bulk RNA-seq and qPCR.
(M) Correlation analysis between the relative expression of *Hif3a* (left), *Fmo2* (middle), and *Wnt10b* (right) mRNA and IFN-γ levels in NAc (n = 10).
(N) The relative expression of *Fabp7* mRNA (n = 8, 9).
(O) ELISA analysis of IFN-γ in peripheral blood (n = 6).
(P–S) The effects of Fabp7 overexpression on synaptic morphology of NAc by Golgi-Cox staining and TEM.
(P) Representative Golgi-Cox staining images; scale bars, 5 μm.
(Q) The number of spines, the proportions of mushroom-like, branched-like, and unclassified spines (n = 6).
(R) Representative TEM images; scale bars, 100 nm.
(S) The number of synapses, the number of asymmetrical synapses, the number of symmetrical synapses, the thickness of the PSD at the thickest part in asymmetrical synapses, the lengths of active zones in symmetrical synapses, and the width of the synaptic cleft in asymmetrical and symmetrical synapses (n = 4).
(T) The counts of scores for withdrawal symptoms 48 h after the last morphine treatment (n = 8).
Data are shown as the mean ± SEM. Data represent two to five independent experiments. $^{*}p < 0.05$, $^{**}p < 0.01$, $^{***}p < 0.001$, $^{****}p < 0.0001$ compared with saline group (A), saline × *Ccr2*^{loxp} group (E, G, and H), saline × scrambled group (I and J) or saline × EGFP group (N, O, Q, S, and T); $^{\#}p < 0.05$, $^{\#\#}p < 0.01$, $^{\#\#\#} < 0.001$. See also Figures 5, 6, and 7.